# Experimental determination of equilibrium nickel isotope fractionation between metal and silicate from 500 °C to 950 °C

Codi Lazar [*], Edward D. Young, Craig E. Manning

*Department of Earth and Space Sciences, University of California at Los Angeles, Los Angeles, CA 90095-1567, USA*

Received 20 October 2011; accepted in revised form 20 February 2012; available online 7 March 2012

## Abstract

The geochemical implications of mass-dependent fractionation of stable Ni isotopes in natural materials are difficult to assess because the inter-mineral equilibrium fractionation factors for Ni are unknown. We report experimentally determined equilibrium fractionation of Ni isotopes between Ni-metal and Ni-talc from 500 °C to 950 °C and 8 to 13 kbar using the three-isotope method. While significant isotope exchange was observed between metal and talc, little or no exchange occurred between Ni-metal and Ni-oxide under similar conditions. These results demonstrate the importance of chemical potential differences between the initial and final phase assemblages in facilitating isotope exchange in the experiments. Metal had greater $^{62}Ni/^{58}Ni$ than talc in all experiments and the equilibrium temperature dependence may be described by the relation $\Delta^{62}Ni_{metal-talc} = 0.25(\pm0.02) \times 10^6/T^2$ ($\pm2se$). Kinetic fractionation resulting from diffusion appeared to perturb isotopic equilibration at long time scales and/or high temperatures. These experiments place constraints on Ni isotope variations observed in natural systems. For example, Ni isotope fractionation between alloy and chondrule in the Ausson meteorite is larger than predicted for an equilibrium process at the canonical metamorphic temperatures of L5 chondrites. At 2500 K, the results imply a difference of 0.04‰ between equilibrated bulk silicate Earth and chondrites, indicating that Ni isotopes are not likely to be useful as tracers of planetary differentiation, unless fractionation occurred by a Rayleigh distillation process involving a well-mixed silicate reservoir.

## 1. INTRODUCTION

Measurable equilibrium inter-mineral fractionation of Fe isotopes at high temperature has been demonstrated in the laboratory (Shahar et al., 2008) and recent studies have revealed mass-dependent isotope fractionation of stable Ni isotopes in meteorites and terrestrial materials (Tanimizu and Hirata, 2006; Cook et al., 2007; Moynier et al., 2007; Steele et al., 2011). Given the similarities in relative mass differences between Fe and Ni isotopes, there is reason to expect that Ni isotopes would also exhibit measurable equilibrium fractionations at high temperatures. Partitioning

between metal and silicate is especially relevant to the prospect of a Ni isotope signature of planetary differentiation. If fractionation of Ni isotopes is sufficiently large between Ni alloy and silicates, metal–silicate equilibration during core formation could have resulted in resolvable differences between bulk silicate Earth (BSE) and chondritic Ni isotope ratios. Equilibrium Ni isotope partitioning between metal and silicate is also potentially useful for characterizing equilibrium conditions in some igneous and metamorphic rocks. Knowledge of the temperature-dependence of equilibrium Ni isotope fractionation between metal and silicate may lead to useful geothermometers for alloy-bearing meteorites and serpentinites.

Experiments and theoretical calculations have suggested that the equilibrium Ni isotope fractionation between $Ni^{+2}$-bearing aqueous complexes may be as high as 1.25‰/amu

---

[*] Corresponding author.
   *E-mail address:* clazar@ciw.edu (C. Lazar).

at 25 °C (Fujii et al., 2011). However, the fractionation factor in the solid metal-silicate system is unknown at any temperature. We applied the three-isotope method to measure the equilibrium fractionation of Ni isotopes between metal and silicate in a series of experiments at high temperatures and pressures. Nickel talc ($Ni_3Si_4O_{10}(OH)_2$, willemseite) was selected as a representative silicate for several practical reasons including ease of physical separation from metal (Section 2.4) and rapid experimental formation (Section 3.3.2). Additionally, metal and talc are stable together in an invariant assemblage that contains no other nickel-bearing phases (Section 4.1). Although Ni talc occurs rarely in nature, the fractionation factor derived from the experimental metal-talc system is likely a reasonable model for equilibrium Ni isotope fractionation in most natural metal–silicate systems. Recent experiments have shown that the inter-mineral fractionation of Si isotopes between metal and silicate melt is analytically indistinguishable from that between metal and olivine (Shahar et al., 2011), suggesting metal-mineral fractionation is similar to metal-melt fractionation. Furthermore, the contrast in the bonding environment of Ni between metal and silicate is much greater than that between endmembers of a metal solid solution series (e.g., Ni° substitution for Fe°) or between octahedral coordination sites of distinct silicate minerals (e.g., ortho versus sheet silicate). The present results yield a measurable temperature-dependent fractionation factor between Ni metal and Ni-talc that can be used to approximate metal–silicate partitioning in general.

## 2. METHODS

In this section, the details of the three-isotope method are described, along with the experimental and analytical techniques used to apply it in the present study.

### 2.1. The three-isotope method

The three-isotope method is a technique used to determine the equilibrium fractionation factor of stable isotopes between two phases. It was originally developed to study solid–fluid oxygen isotope exchange in the quartz-$H_2O$ system (Matsuhisa et al., 1978), and was recently adapted to solid–solid fractionation of non-traditional stable isotopes in studies of Fe isotope exchange between magnetite and fayalite (Shahar et al., 2008) and Si isotope exchange between Fe–Si alloy and silicate melt (Shahar et al., 2009; Shahar et al., 2011). It has also been used to investigate Fe isotope exchange between aqueous ferric chloride complexes (Hill et al., 2009). Central to the technique is the presentation and analysis of data on a three-isotope plot (Fig. 1), so named for the two axes defined by two isotope ratios sharing the same denominator. In the present study deviations in $^{60}Ni/^{58}Ni$ and $^{62}Ni/^{58}Ni$ isotope ratios from a standard in per mil (‰) are used to define three-isotope space. The per mil deviations are expressed in the usual delta notation:

$$\delta^n Ni = \left( \frac{\left(\frac{^n Ni}{^{58} Ni}\right)_{SAMPLE}}{\left(\frac{^n Ni}{^{58} Ni}\right)_{STANDARD}} - 1 \right) \times 1000 \quad (1)$$

where $n = 60$ or 62.

The three-isotope method relies on isotope exchange between a phase (a mineral in our case) spiked with an isotope of interest with another phase with "normal" isotopic composition. The spiked phase lies off the terrestrial fractionation line (TFL) that defines mass-dependent fractionation among the three isotopes of interest. The unspiked phase lies on the TFL. Exchange between the two phases is shown schematically in Fig. 1. In principle, the composition of each mineral shifts over time toward equilibrium isotope ratios. The equilibrium isotope ratios will be co-linear with the bulk composition defined by the two phases along a secondary mass-dependent fractionation line (SFL). An advantage of the three-isotope method is that the isotopic compositions need not actually reach exchange equilibrium in an experiment. Instead, a set of isothermal experiments of different durations, i.e., a time series at constant $T$, yields isotopic compositions that define two straight lines representing the two phases. These lines trend towards their equilibrium values and can be extrapolated to their intersection with the SFL. The difference between these extrapolated intersections is the inter-mineral equilibrium fractionation value ($\Delta$) at a given temperature, e.g., for the present example:

$$\Delta^{62}Ni_{metal-talc} = \delta^{62}Ni_{metal} - \delta^{62}Ni_{talc} \quad (2)$$

where $\delta^{62}Ni_{metal}$ is equal to the value of the open circle in Fig. 1, and $\delta^{62}Ni_{talc}$ is equal to the value of the open square. There are several assumptions implied by this topology, as discussed in Section 4.2.

The extrapolated time series of $\delta^{60}Ni$ and $\delta^{62}Ni$ data (Fig. 1, $t_0$–$t_2$) are fit linearly using the new "York" weighted regression algorithm (Mahon, 1996). Following Shahar et al. (2008), the uncertainties in the slopes and intercepts of the regression analyses are used to calculate $2\sigma$ error envelopes, shown schematically in Fig. 1. The slope of the TFL and SFL, $\beta$, is taken to be 0.5164 based on the expression for equilibrium mass fractionation (Young et al., 2002).

$$\beta = \frac{\left(\frac{1}{m_{58}} - \frac{1}{m_{60}}\right)}{\left(\frac{1}{m_{58}} - \frac{1}{m_{62}}\right)} \quad (3)$$

where $m_i$ is the precise mass of each isotope $i$. The York regression technique is also used to compute linear fits and error envelopes for the temperature versus fractionation data (Section 4.3).

### 2.2. Starting materials and Ni isotope bulk compositions

Starting materials were prepared from spiked and unspiked Ni reservoirs. Nickel metal powder composed of >99.9% $^{58}Ni$ was acquired from Oak Ridge National Laboratory ($^{58}Ni°$). The unspiked Ni metal that lies on the terrestrial fractionation line in three-isotope space ($Ni°_T$) is >99.9% pure partially porous powder sponge (Research Organic/Inorganic Chemical Corp.). Quartz in the experiments is a >99.9% pure floated powder (Fisher Scientific). Spiked NiO was prepared by dissolving a mixture of $Ni°_T$ and $^{58}Ni°$ (1000:1 by mass) in concentrated $HNO_3$. KOH was then added to precipitate spiked $Ni(OH)_2$. After filtering and rinsing repeatedly with distilled $H_2O$, the hydroxide precipitate was gently dried at
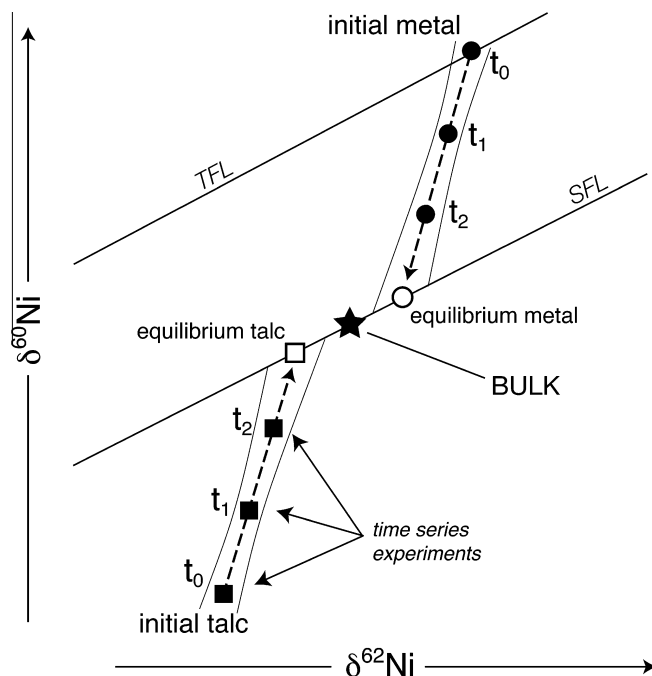
Fig. 1. Schematic diagram of the three-isotope method as applied in the present study, adapted from Shahar et al. (2008). Terrestrial and secondary fractionation lines (TFL and SFL) have slopes of 0.5164 defined by equilibrium mass-dependent fractionation. Filled star = bulk; filled squares = talc; filled circles = metal. Dashed arrows are extrapolated regressions computed for measurements from time $t_0$ to $t_2$. Thin solid lines are $\pm 2\sigma$ error envelopes about the regression line. The equilibrium $\delta$ values (open symbols) are computed as the intersections of the dashed arrows with the SFL defined by slope $\beta$ (Section 2.1) and the bulk composition of the system. The uncertainties in equilibrated $\delta$ values are computed as the intersections of the error envelopes with the SFL.

55 °C and then dehydrated overnight at 300 °C to form medium gray NiO particles. X-ray diffraction analysis of the spiked Ni hydroxide and oxide powders yielded peaks consistent with the respective hydroxide (theophrastite) and oxide (bunsenite) reference diffractograms.

Two types of experiment were performed: metal-oxide exchange and metal-talc exchange. The latter was employed to facilitate Ni isotope exchange by heterogeneous reaction rather than relying on diffusive isotope exchange alone. The starting assemblage of the metal-oxide experiments was $Ni^{\circ}_T$, spiked $Ni(OH)_2$, and pure $H_2O$ (18 megaohm). Petrographic inspection of some preliminary unpublished experiments demonstrated that $Ni(OH)_2$ rapidly decomposes to NiO and $H_2O$ at the experimental conditions, thus the final assemblage in the metal-oxide experiments was metal + oxide + fluid. The starting assemblage in the metal-talc experiments was $Ni^{\circ}_T$, spiked NiO, and quartz at a respective mass ratio of $\sim$1:1:2, plus pure $H_2O$. At the experimental conditions, NiO was consumed to generate Ni-talc, leading to a final assemblage in the metal-talc experiments of metal + talc + quartz + $H_2O$ (Section 4.1).

## 2.3. Piston cylinder experiments

As with Matsuhisa et al., (1978), our experiments were performed at high pressure in a piston cylinder apparatus. Experimental pressures were held constant during each experiment, but varied between experiments from 8 to 13 kbar. We emphasize that $\Delta V$ has a vanishingly small contribution to the energetics of equilibrium Ni isotope fractionation; therefore, isotope equilibrium is expected to be independent of pressure over this pressure range. Moreover, pressure has been shown to enhance the rate and extent of oxygen isotope exchange between quartz and water in previous three isotope experiments (Matthews et al., 1983), a likely reflection of the large increase in quartz solubility with pressure (Manning, 1994). In practical terms, application of pressure decreases the distance between experimental data points and the SFL, with the advantage of decreasing uncertainty in the extrapolation of three-isotope exchange trajectories and increasing the precision of the derived fractionation factors.

Experiments were performed at 500 °C–950 °C for 1 to 4320 min (Table 1). Starting minerals were loaded into Au capsules together with a few milligrams of pure $H_2O$. Au was used because of its low permeability to $H_2$ at the experimental conditions (Eugster and Wones, 1962), permitting the redox-sensitive phase assemblages to buffer oxygen fugacity. The capsules were welded with a carbon electrode, and placed in one-inch diameter NaCl-graphite furnace assemblies (Manning and Boettcher, 1994). The experiments were heated in the piston-cylinder apparatus at a rate of $\sim$20 °C per minute. Temperature was measured with $Pt_{100}$-$Pt_{90}Rh_{10}$ thermocouples (precision of $\pm$3 °C). Temperatures were not corrected for the effect of pressure on emf (Ulmer, 1971). Pressure was monitored via a Heise Bourdon-tube pressure gauge. Experiments were quenched to below 300 °C in less than 30 s. Each post-run capsule was cleaned and weighed, punctured and dried overnight at 110 °C, and then re-weighed to determine the mass of free $H_2O$.

Table 1
Experimental conditions and starting compositions. Weighing uncertainties are zero relative to the reported precision.

| Type | $T$ (°C) | Time (min) | Run name | $P$ (kbar) | Starting mix (type) | (mg) | $Ni_{BULK}$ (μmol) | $H_2O$ in (mg) | $H_2O$[d] out (mg) | %$H_2O$[d] difference | Capsule[e] in (mg) | Capsule[e] out (mg) |
|---|---|---|---|---|---|---|---|---|---|---|---|---|
| Metal-oxide | 800 | 900 | N14 | 10 | inter[a] | 112.58 | 774(12) | 51.96 | 51.96 | 0.0 | 822.85 | 822.83 |
| Metal-oxide | 800 | 1080 | N11 | 10 | sep[b] | 47.73 | 328(5) | 26.00 | 26.01 | 0.0 | 769.85 | 769.84 |
| Metal-oxide | 800 | 1500 | N12 | 13 | sep | ≈45 | 309(5) | 25.82 | 26.02 | 0.8 | 771.63 | 771.62 |
| Metal-oxide | 800 | 2940 | N10 | 11 | sep | ≈45 | 309(5) | 26.02 | 26.00 | −0.1 | 716.89 | 716.90 |
| Metal-talc | 500 | 150 | N26 | 8 | C[c] | 16.29 | 112(2) | 7.19 | 6.74 | −6.2 | 336.14 | 336.12 |
| Metal-talc | 500 | 180 | N28 | 9 | C | 8.51 | 58(1) | 2.78 | 2.62 | −6.0 | 310.43 | 310.42 |
| Metal-talc | 500 | 1080 | N30 | 10 | C | 15.10 | 104(2) | 5.80 | 5.38 | −7.3 | 336.50 | 336.48 |
| Metal-talc | 500 | 4320 | N32 | 10 | C | 14.91 | 103(2) | 7.55 | 7.09 | −6.1 | 324.55 | 324.53 |
| Metal-talc | 615 | 120 | N31 | 10 | C | 9.77 | 67(1) | 3.01 | 2.74 | −9.0 | 314.25 | 314.24 |
| Metal-talc | 615 | 300 | N33 | 12 | C | 9.01 | 62(1) | 3.10 | 2.82 | −8.9 | 316.39 | 316.38 |
| Metal-talc | 615 | 1380 | N34 | 12 | C | 10.64 | 73(1) | 2.17 | 2.18 | +1 | 318.44 | 318.38 |
| Metal-talc | 800 | 20 | N19 | 10 | C | 15.41 | 106(2) | 5.16 | 4.48 | −13.3 | 321.61 | 321.05 |
| Metal-talc | 800 | 40 | N21 | 11 | C | 16.94 | 116(2) | 2.75 | n.d. | n.d. | 318.16 | 318.04 |
| Metal-talc | 800 | 100 | N18 | 10 | C | 16.19 | 111(2) | 2.37 | n.d. | n.d. | 262.27 | 262.26 |
| Metal-talc | 800 | 1110 | N20 | 10 | C | 14.47 | 103(2) | 4.72 | 4.52 | −4.2 | 321.33 | 321.32 |
| Metal-talc | 900 | 10 | N27 | 12 | C | 11.09 | 76(1) | 5.58 | 5.40 | −3.1 | 276.07 | 276.05 |
| Metal-talc | 900 | 45 | N29 | 12 | C | 11.80 | 81(1) | 6.87 | 6.72 | −2.1 | 277.02 | 277.01 |
| Metal-talc | 950 | 1 | N24 | 10 | C | 15.35 | 106(2) | 7.17 | n.d. | n.d. | 338.39 | 338.88 |
| Metal-talc | 950 | 10 | N25 | 10 | C | 14.59 | 100(2) | 6.23 | 6.07 | −2.6 | 328.73 | 328.73 |

[a] *inter*: Large spiked $Ni(OH)_2$ grains chunks immersed in $Ni°_T$ powder.
[b] *sep*: Spiked $Ni(OH)_2$ segregated from $Ni°_{TFL}$ in an unwelded Pt capsule.
[c] *C*: $Ni°_T$ + spiked oxide + quartz (1:1:2 wt. ratio).
[d] Free water.
[e] Welded Au capsule plus contents.

## 2.4. Isotope ratio analyses

Measurement of inter-mineral isotope fractionation of Ni requires complete separation of the nickeliferous phases prior to mass spectrometric analysis. The starting assemblage of the metal-talc experiments was loaded into the Au capsule as a loose powder and the post-run products were finely intermingled in a heterogeneous aggregate. Separation was straightforward because Ni metal is ferromagnetic, while Ni-talc and quartz are not. With the aid of a magnet, light grinding in an agate mortar under a stream of acetone was sufficient to wash away talc and quartz from the metal. This procedure was repeated until the purity of each separate could be optically confirmed with a binocular microscope, facilitated by the contrast between gray metal and the light green talc-quartz mixture. Ni is highly incompatible in quartz, eliminating the need for physical separation of talc and quartz for Ni isotope ratio analysis of talc.

Since NiO is weakly magnetic, the metal-oxide experiments were configured to permit post-run phase separation without relying on a magnet. Spiked $Ni(OH)_2$ was either segregated from $Ni°_T$ by placing it inside an unwelded Pt capsule, or loaded as large chunks (∼3–5 mm) within a matrix of fine $Ni°_T$ metal powder. Although some metal particles formed *in situ* within these oxide chunks, the particles were sufficiently sparse to be easily removed by hand picking.

To prepare for isotopic analysis, run product separates were digested overnight in Savillex (Teflon) beakers at 120 °C. Ni metal and NiO were dissolved in concentrated $HNO_3$. The talc-quartz mixtures were dissolved in a 1:1 mixture of concentrated $HNO_3$ and concentrated HF. No chromatographic purification was required because the starting minerals were of high purity, containing only Ni, Si, and O. No Au from surrounding capsule material was detected in the reacted Ni metal grains. Silicon in talc and

Table 2
Mean isotopic compositions of starting materials.

| | $\delta^{60}Ni$ | Uncertainty | $\delta^{62}Ni$ | Uncertainty | Corr | $S$ | $N$ |
|---|---|---|---|---|---|---|---|
| $Ni°_{TFL}$/zero-enrichment[a] | −0.003 | 0.015 | −0.001 | 0.034 | 0.624 | 22 | 78 |
| SRM986 standard[a] | 0.098 | 0.007 | 0.186 | 0.021 | 0.545 | 15 | 70 |
| Spiked NiO[b] | −27.836 | 0.005 | −27.881 | 0.008 | −0.146 | 1 | 10 |
| Starting mixture C[b] | −12.668 | 0.005 | −12.691 | 0.015 | 0.822 | 1 | 5 |

$S$ = number of samples. $N$ = total number of analyses. Corr = correlation coefficient of cycle values if $S = 1$, or correlation coefficient of sample values if $S > 1$.
[a] Uncertainty = ±2sd.
[b] Uncertainty = ±2se.

quartz was removed by volatilization of $SiF_{4(g)}$. After sample digestion, the solutions were dried slowly at 120 °C to a bright green $Ni(OH)_2$ precipitate. Prior to isotope analysis all materials were dissolved at room temperature in ultra-pure 2% $HNO_3$.

Isotope analyses were performed on the UCLA Thermo-Finnigan Neptune™ multicollector inductively coupled plasma mass spectrometer (MC-ICPMS). Analyses were performed at a mass resolving power (m/Δm) of 5500–6500, sufficient to achieve adequate separation of $^{58}Ni^+$ from $^{40}Ar^{18}O^+$. Further analytical details are provided in the Electronic Annex. Analyses are reported for the three most abundant Ni isotopes of masses 58, 60, and 62 amu, with relative terrestrial abundances of 0.68, 0.26, and 0.04 (De Laeter et al., 2003). Delta values, $\delta^{60}Ni$ and $\delta^{62}Ni$, were computed relative to NIST SRM-986 metal powder via Eq. (1). Instrumental mass bias was corrected using sample-standard bracketing with $Ni^{\circ}_T$. The external precision (±2σ) for the analyses reported here are ±0.007‰ for $\delta^{60}Ni$ and ±0.021‰ for $\delta^{62}Ni$ (Fig. EA1, Electronic annex). Isotopic compositions of the starting materials are reported in Table 2.

## 3. RESULTS

### 3.1. Textural evidence for reactions

Scanning-electron microscopy (SEM) and reflected-light petrography of the metal-oxide experiments revealed no observable textural or mineralogical changes between the
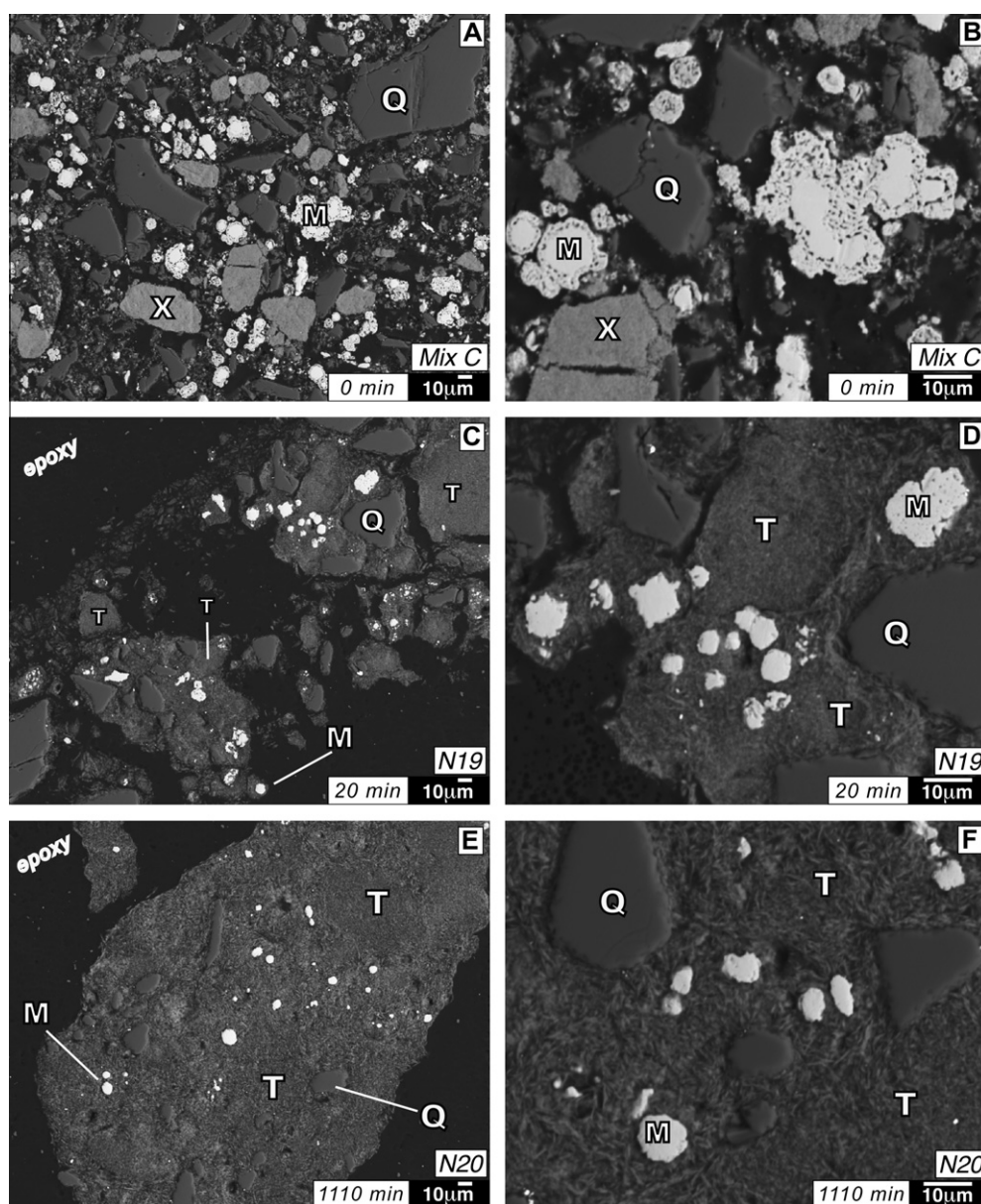


Fig. 2. Backscattered electron images of metal-talc starting mixture C (top panels A and B) and 800 °C metal-talc experiments N19 (20 min, C and D) and N20 (1110 min, E and F). T = talc, Q = quartz, M = metal, X = spiked NiO.
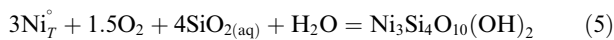
initial and final metal-oxide mixtures. In contrast, the metal-talc products and textures evolved unambiguously with time and temperature. In general, as time and temperature increased, the metal-talc run products became more talc-rich and metal-poor. No NiO or $Ni(OH)_2$ particles were observed in the products of any metal-talc experiment.

The textural evolution in metal-talc experiments with time was assessed by SEM analysis (Fig. 2) and point counting (Table 3) of 800 °C run products. Comparison of the initial assemblage to run products after 20 min (run N19) and 1110 min (run N20) shows that even after just 20 min, no reactant NiO particles were observed in the charge. Between 20 and 1110 min, the relative modal abundance and average grain size of talc increased. From 0 to 1110 min, the shape of the quartz and metal grains became more rounded, and porous mantles of the metal particles disappeared. The relative modal abundances of metal and quartz decreased from 0 to 1110 min.

The petrographic observations are consistent with two mechanisms of talc formation: rapid consumption of spiked NiO by the reaction

$$3NiO_{spiked} + 4SiO_{2(aq)} + H_2O = Ni_3Si_4O_{10}(OH)_2 (talc) \quad (4)$$
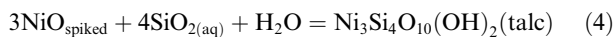
and slower oxidation of $Ni°_T$ via the reaction

$$3Ni°_T + 1.5O_2 + 4SiO_{2(aq)} + H_2O = Ni_3Si_4O_{10}(OH)_2 \quad (5)$$

Talc formation in the metal-talc experiments by Reactions (4) and (5) is consistent with the observation that the output $H_2O$ was 2–10% less than the input $H_2O$ (Table 1). Moreover, water consumption was 2–3X higher in the 900 °C and 950 °C experiments than in the 500 °C and 615 °C experiments, consistent with the petrographic observation of more extensive talc formation at high temperature.

By contrast, the change in free $H_2O$ in the metal-oxide experiments was nearly zero, consistent with the absence of a hydrous mineral.

### 3.2. Ni–Au alloying

Talc was not the only nickel sink in the experiments. The color of the inner capsule walls evolved with time and temperature from metallic gold to metallic gray, reflecting progressive Ni dissolution into the capsule. Electron microprobe analyses of the inner capsule walls showed that Ni–Au alloying occurred in each experiment, even in the shortest 500 °C runs which displayed no discoloration. Selected compositional profiles are shown in Fig. 3. We observed neither a bi-phase quench region within the capsule wall nor globular metal particles in the capsule contents, indicating that binary melting did not occur.
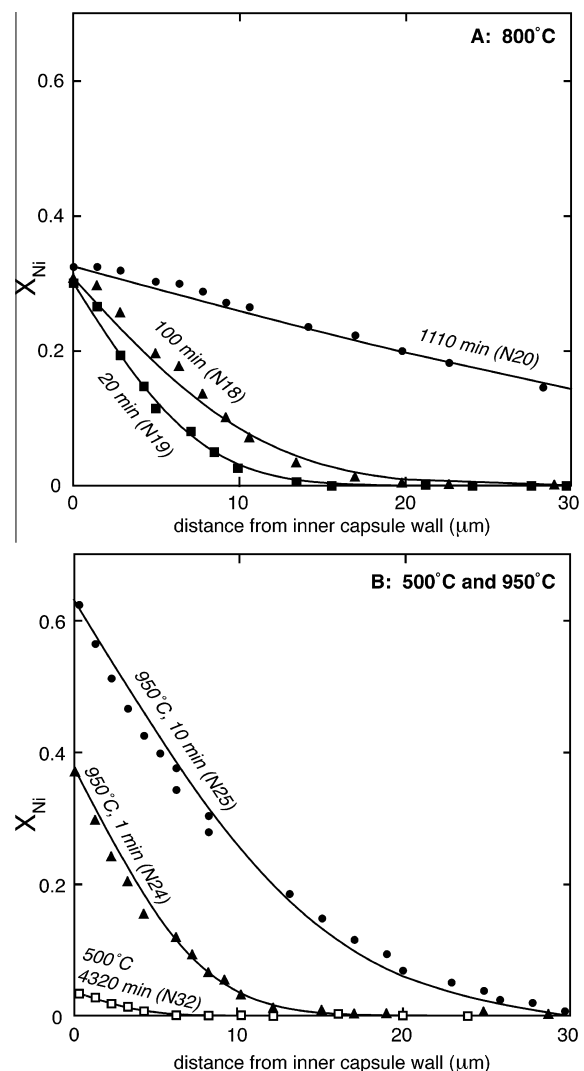


Fig. 3. Examples of Ni concentration (in mole fraction, $X_{Ni}$) profiles in Au capsule walls for metal-talc experiments. Solid lines are curves representing best fits with Eq. (EA2). Error bars are not visible at this scale.

Table 3
Point count data and mass balance calculation for experiments N19 and N20.

| | N19 (800 °C, 20 min) | N20 (800 °C, 1110 min) |
|---|---|---|
| | Moles of reactants (µmol)[1] | |
| $Ni°_{TFL}$ | 57(4) | 54(4) |
| Spiked NiO | 49(3) | 46(3) |
| Quartz | 140(23) | 131(22) |
| | Point count of run products (vol.%)[b] | |
| Ni° | 5(2) | 2(1) |
| Talc | 74(4) | 90(5) |
| Quartz | 21(3) | 8(2) |
| | Observed moles of products (µmol) | |
| Ni°particles | 33(15) | 11(6) |
| Ni° in Au[c] | 5(2) | 36(8) |
| Talc | 24(5) | 24(2) |
| Quartz | 40(11) | 13(3) |
| | Total Ni (µmol) | |
| Reactants[a] | 106(5) | 100(5) |
| Products[d] | 109(22) | 119(11) |

[a] Derived from Table 1.
[b] From Fig. 2, excludes Ni in Au.
[c] $Ni_{BULK}$ (Table 1) × %$Ni_{ALLOY}$ (Table EA1).
[d] Total Ni = ($3N_{talc} + N_{alloy} + N_{particles}$), where $N$ = number of moles.

### 3.3. Isotope Exchange

#### 3.3.1. Metal-oxide experiments

In the metal-oxide experiments (Table 4), the isotopic compositions of the endmember phases did not change appreciably toward the SFL (Fig. 4A), preventing a statistically meaningful application of the three-isotope method. Some minor isotopic exchange occurred at a small scale: e.g., almost all delta values of both phases were greater than the initial compositions (Fig. 4B and C). Isotope fractionation in the metal data followed mass dependence along the TFL, and spanned a $\delta^{62}$Ni range of 0.5‰. The trend

from the initial value toward heavy isotope enrichment may have occurred due to kinetic fractionation during diffusive loss of metal to the capsule (Roskosz et al., 2006) or during localized oxidation to NiO depleted in the higher mass Ni isotopes. The oxide data were distributed over a $\delta^{62}$Ni range of ~2‰, roughly clustered along a slope of unity, consistent with a path towards equilibration in three-isotope space. However, the extent of reaction was too small for a statistically significant extrapolation toward the SFL and could not be used to constrain the sign or magnitude of fractionation between metal and oxide. Note that the bulk composition in Fig. 4A is approximate, because

Table 4
Results of metal-oxide experiments, 800 °C.

| Sample | Analysis date | Time (hrs) | Phase | $\delta^{60}$Ni | ±2se | $\delta^{62}$Ni | ±2se |
|---|---|---|---|---|---|---|---|
| N14-m1 | 05/29/09 | 15 | Metal | 0.010 | 0.009 | 0.066 | 0.018 |
| N14-m2 | 05/29/09 | 15 | Metal | 0.010 | 0.006 | 0.028 | 0.024 |
| N11-m1 | 12/18/08 | 18 | Metal | 0.018 | 0.034 | 0.040 | 0.076 |
| N11-m2 | 12/18/08 | 18 | Metal | 0.082 | 0.023 | 0.167 | 0.044 |
| N12-m1 | 12/18/08 | 25 | Metal | 0.082 | 0.025 | 0.166 | 0.049 |
| N12-m2 | 12/18/08 | 25 | Metal | 0.146 | 0.039 | 0.280 | 0.078 |
| N10-m1 | 12/17/08 | 49 | Metal | 0.155 | 0.025 | 0.333 | 0.045 |
| N10-m2 | 12/17/08 | 49 | Metal | 0.183 | 0.023 | 0.466 | 0.039 |
| N14-o | 05/29/09 | 15 | Oxide | −26.863 | 0.022 | −26.861 | 0.046 |
| N11-o1 | 12/18/08 | 18 | Oxide | −27.459 | 0.027 | −27.547 | 0.066 |
| N11-o2 | 12/18/08 | 18 | Oxide | −27.345 | 0.012 | −27.351 | 0.019 |
| N11-o3 | 12/18/08 | 18 | Oxide | −27.351 | 0.017 | −27.304 | 0.038 |
| N11-o4 | 12/18/08 | 18 | Oxide | −27.622 | 0.012 | −27.548 | 0.026 |
| N11-o5 | 12/18/08 | 18 | Oxide | −26.757 | 0.022 | −26.778 | 0.044 |
| N12-o1 | 12/18/08 | 25 | Oxide | −27.486 | 0.037 | −27.449 | 0.073 |
| N12-o2 | 12/18/08 | 25 | Oxide | −27.632 | 0.028 | −27.707 | 0.061 |
| N12-o3 | 12/18/08 | 25 | Oxide | −27.736 | 0.029 | −27.762 | 0.061 |
| N12-o4 | 12/18/08 | 25 | Oxide | −27.402 | 0.029 | −27.216 | 0.060 |
| N12-o5 | 12/18/08 | 25 | Oxide | −27.632 | 0.022 | −27.619 | 0.046 |
| N10-oA | 12/17/08 | 49 | Oxide | −27.383 | 0.023 | −27.452 | 0.051 |
| N10-oB | 12/18/08 | 49 | Oxide | −27.295 | 0.041 | −27.354 | 0.084 |
| N10-oC | 12/18/08 | 49 | Oxide | −27.313 | 0.028 | −27.381 | 0.059 |
| N10-o1 | 12/17/08 | 49 | Oxide | −28.090 | 0.038 | −28.406 | 0.085 |
| N10-o2 | 12/17/08 | 49 | Oxide | −27.775 | 0.019 | −27.844 | 0.042 |
| N10-o3 | 12/18/08 | 49 | Oxide | −27.858 | 0.059 | −28.005 | 0.119 |
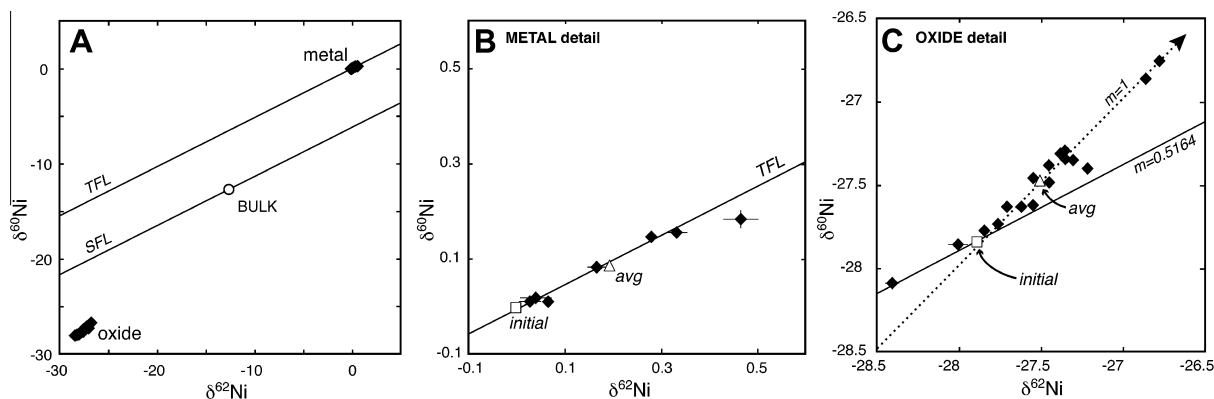


Fig. 4. Metal-oxide experimental results, $\delta^{60}$Ni versus $\delta^{62}$Ni. (A) Three-isotope plot of metal and oxide experiments. Open circle = bulk composition. (B and C) Enlarged views of metal and oxide data in A, respectively. Open squares = initial endmember compositions with uncertainties from Table 2. Open triangles = average experimental compositions. The solid line in C is a mass dependent line passing through the initial oxide composition. Dotted arrow in C has a unity slope reflecting mixing between spiked oxide and unspiked metal in the experiments. Individual error bars are ±2se.

Table 5
Isotopic results of metal–talc experiments, 500 °C–950 °C.

| T (°C) | Sample name | Analysis date | Phase | Time (min) | $\delta^{60}$Ni | ±2se | $\delta^{62}$Ni | ±2se | Corr | n | $I/I_S$ |
|---|---|---|---|---|---|---|---|---|---|---|---|
| 500 | N28mB | 01/22/10 | Metal | 150 | −1.748 | 0.021 | −1.713 | 0.009 | 0.613 | 3 | 0.7 |
| 500 | N32mA | 06/08/10 | Metal | 180 | −2.488 | 0.020 | −2.515 | 0.038 | 0.953 | 5 | 0.9 |
| 500 | N32mB1 | 06/07/10 | Metal | 180 | −2.758 | 0.010 | −2.737 | 0.008 | 0.900 | 4 | 1.0 |
| 500 | N32mB2 | 06/17/10 | Metal | 180 | −2.849 | 0.013 | −2.912 | 0.028 | 0.972 | 5 | 1.1 |
| 500 | N30mA | 01/22/10 | Metal | 1080 | −3.593 | 0.007 | −3.524 | 0.016 | 0.839 | 5 | 1.1 |
| 500 | N30mB | 01/24/10 | Metal | 1080 | −3.591 | 0.006 | −3.538 | 0.008 | −0.067 | 5 | 1.1 |
| 500 | N26mA | 02/26/10 | Metal | 4320 | −4.142 | 0.008 | −4.098 | 0.008 | 0.564 | 5 | 0.9 |
| 500 | N26mB | 06/15/10 | Metal | 4320 | −4.139 | 0.004 | −4.114 | 0.012 | 0.576 | 5 | 1.0 |
| 500 | N26mC | 06/15/10 | Metal | 4320 | −4.152 | 0.005 | −4.122 | 0.023 | 0.544 | 5 | 0.9 |
| 500 | N28sB | 01/22/10 | Talc | 150 | −17.297 | 0.011 | −17.684 | 0.017 | 0.836 | 4 | 0.5 |
| 500 | N32sA | 06/07/10 | Talc | 180 | −17.011 | 0.007 | −17.038 | 0.018 | 0.298 | 4 | 1.0 |
| 500 | N32sB | 06/08/10 | Talc | 180 | −16.964 | 0.003 | −17.006 | 0.009 | −0.472 | 5 | 0.8 |
| 500 | N30sA | 01/22/10 | Talc | 1080 | −14.788 | 0.007 | −14.793 | 0.014 | 0.539 | 4 | 0.8 |
| 500 | N30sB | 01/24/10 | Talc | 1080 | −14.902 | 0.008 | −14.983 | 0.011 | 0.739 | 4 | 0.7 |
| 500 | N26sA | 02/26/10 | Talc | 4320 | −15.085 | 0.005 | −15.103 | 0.011 | −0.647 | 5 | 0.9 |
| 500 | N26sB | 06/15/10 | Talc | 4320 | −15.094 | 0.006 | −15.115 | 0.012 | 0.661 | 5 | 1.0 |
| 500 | N26sC | 06/15/10 | Talc | 4320 | −15.093 | 0.007 | −15.124 | 0.018 | 0.755 | 5 | 1.0 |
| 615 | N33mA | 06/07/10 | Metal | 120 | −4.171 | 0.007 | −4.163 | 0.015 | 0.875 | 4 | 1.0 |
| 615 | N33mB | 06/08/10 | Metal | 120 | −3.539 | 0.008 | −3.518 | 0.022 | 0.370 | 5 | 1.0 |
| 615 | N34mA | 06/09/10 | Metal | 300 | −3.618 | 0.008 | −3.574 | 0.017 | 0.666 | 5 | 1.0 |
| 615 | N34mB1 | 06/08/10 | Metal | 300 | −3.559 | 0.010 | −3.517 | 0.020 | 0.312 | 4 | 1.0 |
| 615 | N34mB2 | 06/15/10 | Metal | 300 | −3.668 | 0.008 | −3.633 | 0.014 | 0.803 | 5 | 1.0 |
| 615 | N31mA | 06/08/10 | Metal | 1380 | −4.123 | 0.009 | −4.078 | 0.021 | 0.898 | 5 | 1.0 |
| 615 | N31mB1 | 06/07/10 | Metal | 1380 | −4.574 | 0.007 | −4.546 | 0.026 | 1.000 | 3 | 1.0 |
| 615 | N31mB2 | 06/15/10 | Metal | 1380 | −4.572 | 0.009 | −4.524 | 0.021 | 0.392 | 5 | 0.9 |
| 615 | N33sA | 06/08/10 | Talc | 120 | −15.881 | 0.005 | −15.913 | 0.007 | 0.646 | 5 | 1.0 |
| 615 | N33sB | 06/09/10 | Talc | 120 | −16.313 | 0.005 | −16.348 | 0.004 | 0.648 | 5 | 0.9 |
| 615 | N34sA | 06/08/10 | Talc | 300 | −15.210 | 0.004 | −15.240 | 0.012 | −0.196 | 5 | 1.0 |
| 615 | N34sB | 06/09/10 | Talc | 300 | −15.262 | 0.009 | −15.359 | 0.016 | 0.650 | 5 | 0.9 |
| 615 | N31sA | 06/07/10 | Talc | 1380 | −14.962 | 0.003 | −14.972 | 0.011 | 0.471 | 5 | 0.9 |
| 615 | N31sB | 06/08/10 | Talc | 1380 | −14.312 | 0.007 | −14.332 | 0.008 | 0.435 | 5 | 0.9 |
| 800 | N19mA1 | 10/28/09 | Metal | 20 | −6.607 | 0.010 | −6.562 | 0.020 | 0.103 | 1 | 0.9 |
| 800 | N19mA2 | 10/29/09 | Metal | 20 | −6.629 | 0.008 | −6.583 | 0.015 | 0.393 | 5 | 1.0 |
| 800 | N19mB | 11/04/09 | Metal | 20 | −6.582 | 0.004 | −6.531 | 0.019 | 0.803 | 5 | 1.0 |
| 800 | N21mA1 | 10/28/09 | Metal | 40 | −7.360 | 0.008 | −7.321 | 0.018 | 0.334 | 1 | 0.9 |
| 800 | N21mA2 | 10/30/09 | Metal | 40 | −7.357 | 0.005 | −7.324 | 0.015 | 0.248 | 5 | 1.1 |
| 800 | N21mB | 11/04/09 | Metal | 40 | −7.344 | 0.009 | −7.299 | 0.014 | 0.903 | 5 | 1.0 |
| 800 | N18m | 08/13/09 | Metal | 100 | −8.873 | 0.009 | −8.699 | 0.024 | 0.058 | 1 | 0.9 |
| 800 | N18mA | 11/04/09 | Metal | 100 | −8.968 | 0.007 | −8.907 | 0.015 | 0.725 | 5 | 0.9 |
| 800 | N18mB1 | 08/14/09 | Metal | 100 | −8.855 | 0.024 | −8.698 | 0.044 | 1.000 | 2 | 0.9 |
| 800 | N18mB2 | 11/04/09 | Metal | 100 | −8.861 | 0.018 | −8.777 | 0.019 | 0.819 | 5 | 1.0 |
| 800 | N20mA1 | 10/28/09 | Metal | 1110 | −7.641 | 0.011 | −7.407 | 0.021 | 0.705 | 1 | 0.9 |
| 800 | N20mA2 | 10/29/09 | Metal | 1110 | −7.647 | 0.005 | −7.393 | 0.013 | 0.958 | 5 | 1.1 |
| 800 | N20mB | 11/04/09 | Metal | 1110 | −7.560 | 0.005 | −7.263 | 0.011 | 0.194 | 5 | 0.9 |
| 800 | N19sAB1 | 10/28/09 | Talc | 20 | −16.202 | 0.022 | −16.334 | 0.038 | 0.794 | 1 | 0.9 |
| 800 | N19sAB2 | 10/29/09 | Talc | 20 | −16.205 | 0.034 | −16.356 | 0.068 | 1.000 | 2 | 1.1 |
| 800 | N19sC | 10/30/09 | Talc | 20 | −16.282 | 0.013 | −16.482 | 0.037 | 0.888 | 5 | 1.1 |
| 800 | N21sA1 | 10/28/09 | Talc | 40 | −14.888 | 0.008 | −14.830 | 0.026 | 0.307 | 1 | 0.9 |
| 800 | N21sA2 | 10/29/09 | Talc | 40 | −14.922 | 0.009 | −14.906 | 0.013 | 0.483 | 5 | 1.1 |
| 800 | N21sB | 10/30/09 | Talc | 40 | −14.687 | 0.007 | −14.672 | 0.012 | −0.739 | 5 | 1.1 |
| 800 | N21sC | 11/04/09 | Talc | 40 | −14.949 | 0.008 | −14.915 | 0.015 | 0.731 | 5 | 1.0 |
| 800 | N18s1 | 08/13/09 | Talc | 100 | −16.079 | 0.010 | −15.992 | 0.025 | 0.555 | 1 | 1.0 |
| 800 | N18s2 | 11/04/09 | Talc | 100 | −16.135 | 0.011 | −16.070 | 0.035 | 0.743 | 5 | 0.7 |
| 800 | N20sC | 10/30/09 | Talc | 1110 | −13.019 | 0.005 | −13.195 | 0.013 | 0.698 | 5 | 0.5 |
| 900 | N29mC | 06/08/10 | Metal | 10 | −6.874 | 0.004 | −6.850 | 0.012 | 0.161 | 5 | 1.0 |
| 900 | N27mA | 02/26/10 | Metal | 45 | −7.314 | 0.003 | −7.230 | 0.011 | 0.660 | 5 | 0.9 |
| 900 | N29sB | 06/09/10 | Talc | 10 | −13.756 | 0.025 | −13.754 | 0.047 | 0.966 | 4 | 1.0 |
| 900 | N29sC | 06/08/10 | Talc | 10 | −14.384 | 0.006 | −14.360 | 0.006 | 0.906 | 5 | 1.0 |
| 900 | N27sA | 02/26/10 | Talc | 45 | −12.310 | 0.004 | −12.285 | 0.009 | 0.051 | 5 | 0.9 |

Table 5 (*continued*)

| T ( °C) | Sample name | Analysis date | Phase | Time (min) | $\delta^{60}Ni$ | $\pm 2se$ | $\delta^{62}Ni$ | $\pm 2se$ | Corr | n | $I/I_S$ |
|---|---|---|---|---|---|---|---|---|---|---|---|
| 900 | N27sC | 06/15/10 | Talc | 45 | −12.875 | 0.002 | −12.795 | 0.011 | 0.544 | 5 | 1.0 |
| 950 | N24mA | 01/23/10 | Metal | 1 | −6.053 | 0.005 | −6.026 | 0.023 | 0.537 | 5 | 0.9 |
| 950 | N24mB | 01/22/10 | Metal | 1 | −6.072 | 0.011 | −6.021 | 0.014 | 0.739 | 5 | 1.0 |
| 950 | N25mA | 01/22/10 | Metal | 10 | −6.638 | 0.004 | −6.578 | 0.015 | 0.275 | 5 | 0.9 |
| 950 | N25mB | 01/23/10 | Metal | 10 | −6.662 | 0.007 | −6.601 | 0.016 | 0.726 | 5 | 1.0 |
| 950 | N24sA | 01/23/10 | Talc | 1 | −14.278 | 0.008 | −14.317 | 0.011 | 0.986 | 5 | 1.1 |
| 950 | N24sB | 01/22/10 | Talc | 1 | −14.222 | 0.005 | −14.211 | 0.010 | 0.430 | 5 | 0.8 |
| 950 | N25sA | 01/22/10 | Talc | 10 | −12.588 | 0.007 | −12.535 | 0.016 | 0.724 | 5 | 0.8 |
| 950 | N25sB | 01/23/10 | Talc | 10 | −13.171 | 0.010 | −13.121 | 0.021 | 0.837 | 5 | 1.0 |

Corr = correlation coefficient of *n* repeat analyses. $I/I_S$ = sample-standard intensity ratio (Section EA1).

the absence of metal-oxide exchange rendered its precise measurement unnecessary.

### 3.3.2. Metal-talc experiments

In contrast to the metal-oxide results, the metal-talc data revealed systematic and extensive inter-mineral isotopic exchange (Table 5, Figs. 5 and 6). At all temperatures, metal and talc evolved isotopically toward the SFL, permitting a statistically significant application of the three isotope method (Table 6). The extent of exchange ($\xi$) for each phase generally increased with time and temperature and was computed as

$$\xi_{metal} = (\delta^n Ni_{metal} - \delta^n Ni_{metal,initial})/(\delta^n Ni_{bulk} - \delta^n Ni_{metal,initial}) \quad (6)$$

$$\xi_{talc} = (\delta^n Ni_{talc} - \delta^n Ni_{talc,initial})/(\delta^n Ni_{bulk} - \delta^n Ni_{talc,initial}) \quad (7)$$

where $\delta^n Ni_{bulk}$ is the bulk composition of the entire system as represented by MC-ICP-MS measurements of starting mixture C (Table 2). A plot of $\xi_{metal}$ versus $\xi_{talc}$ (Fig. 7) shows more extensive exchange in talc relative to metal. The extent of talc exchange exceeded 0.6 in most experiments, while that of metal was in most cases below 0.6. This illustrates the utility of the three-isotope method: metal never evolved to a value on the SFL, presumably because of the larger concentration of Ni involved, thus extrapolation of its exchange vector was always required to calculate the equilibrium SFL intersection.

## 4. DISCUSSION

### 4.1. Isotopic exchange mechanism

Isotopic exchange between the nickeliferous phases was significant in the metal-talc experiments but virtually absent in the metal-oxide experiments. In addition, the metal-talc starting materials reacted to a new phase assemblage, but the metal-oxide starting assemblage was unchanged. This suggests a link between the mechanisms leading to chemical and isotopic equilibration, and implies that isotopic exchange is more extensive when the chemical potential gradient between the initial and final assemblages is sufficiently high to drive new mineral growth.

The fact that the initial and final assemblages of the metal-oxide experiments were identical suggests that over the time scale of the experiments, there was no significant progress in either direction of the reaction

$$2Ni^{\circ} + O_2 = 2NiO \quad (8)$$

This equilibrium represents the well-known nickel-nickel oxide (NNO) oxygen fugacity ($fO_2$) buffer. That the final assemblage was metal + oxide + fluid suggests that the initial ambient $fO_2$ in the metal-oxide capsules was close to NNO, and that the initial assemblage was stable at the experimental conditions. This is consistent with independent results, which show that the intrinsic $fO_2$ of unbuffered piston-cylinder experiments with our furnace-assembly design is approximately equal to the NNO buffer (Newton and Manning, 2005).

The results of the metal-oxide (MX) experiments can be contrasted with those of the metal-talc (MT) experiments using a diagram showing phase relations in the system Ni—Si—O—H at 900 °C and 10 kbar, with $H_2O$ in excess (Fig. 8). Whereas the initial (i) and final (f) positions of the MX assemblage remained at a fixed point in terms of fluid composition and $fO_2$, the position of the initially unstable assemblage, $MT^i$, evolve during runs to $MT^f$. The location of $MT^i$ in Fig. 8 reflects the starting assemblage of quartz + Ni° + NiO + $H_2O$, and projects onto the Ni°-talc-quartz phase boundary at $fO_2 \sim$ NNO, even though talc is not present. This assumption is based on independent experimental evidence, which indicates that quartz dissolves rapidly at high pressure and temperature (Manning, 1994; Newton and Manning, 2008). This implies that $SiO_2$ composition equilibrates with quartz within minutes, probably more rapidly than the attending reactions among the minerals. The location of $MT^f$ represents the final stable assemblage at the invariant point defined by the coexistence of Ni-talc, quartz, metal, and fluid, which fixes $fO_2$ approximately one log unit below that of $MT^i$. The arrow illustrates the schematic path from initial to final assemblages and is consistent with four petrographic observations. First, the system was constrained to the quartz saturation surface because quartz was present in the initial and final assemblages of every experiment. Second, no olivine was observed in any
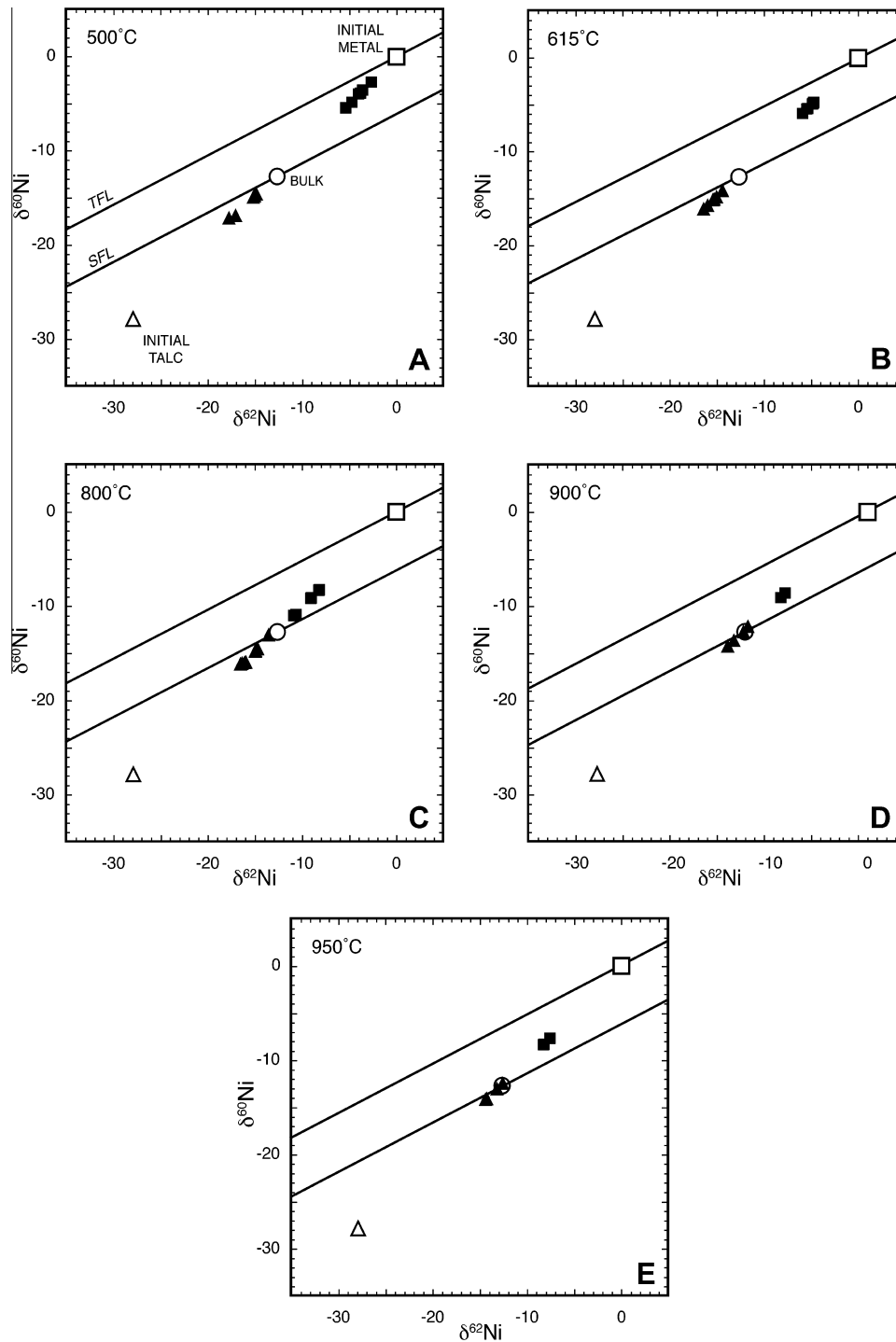
Fig. 5. Metal-talc experimental results, $\delta^{60}$Ni versus $\delta^{62}$Ni. Open triangles = initial talc; Open squares = initial metal; Open circles = measured bulk composition (Table 2); Filled triangles = exchanged talc; Filled squares = exchanged metal. Error bars ($\pm$2se) are smaller than the symbols at this scale.

experiment, consistent with the restriction of silica activity to quartz saturation. Third, Ni° was consumed to generate talc necessarily driving the system to lower $fO_2$ (Reaction (5)). Fourth, the final assemblage was always observed to be the stable invariant assemblage quartz + Ni° + Ni-talc + $H_2O$ at $MT^f$. Note that the same topological relation-

ships apply at all of the experimental conditions, though $fO_2$ and the $SiO_2$ concentrations will differ.

The chemical potential gradient between $MT^i$ and $MT^f$ illustrates the key contrast between the metal-oxide and metal-talc experiments. In the absence of a driving force for new mineral growth in the metal-oxide experiments, Ni
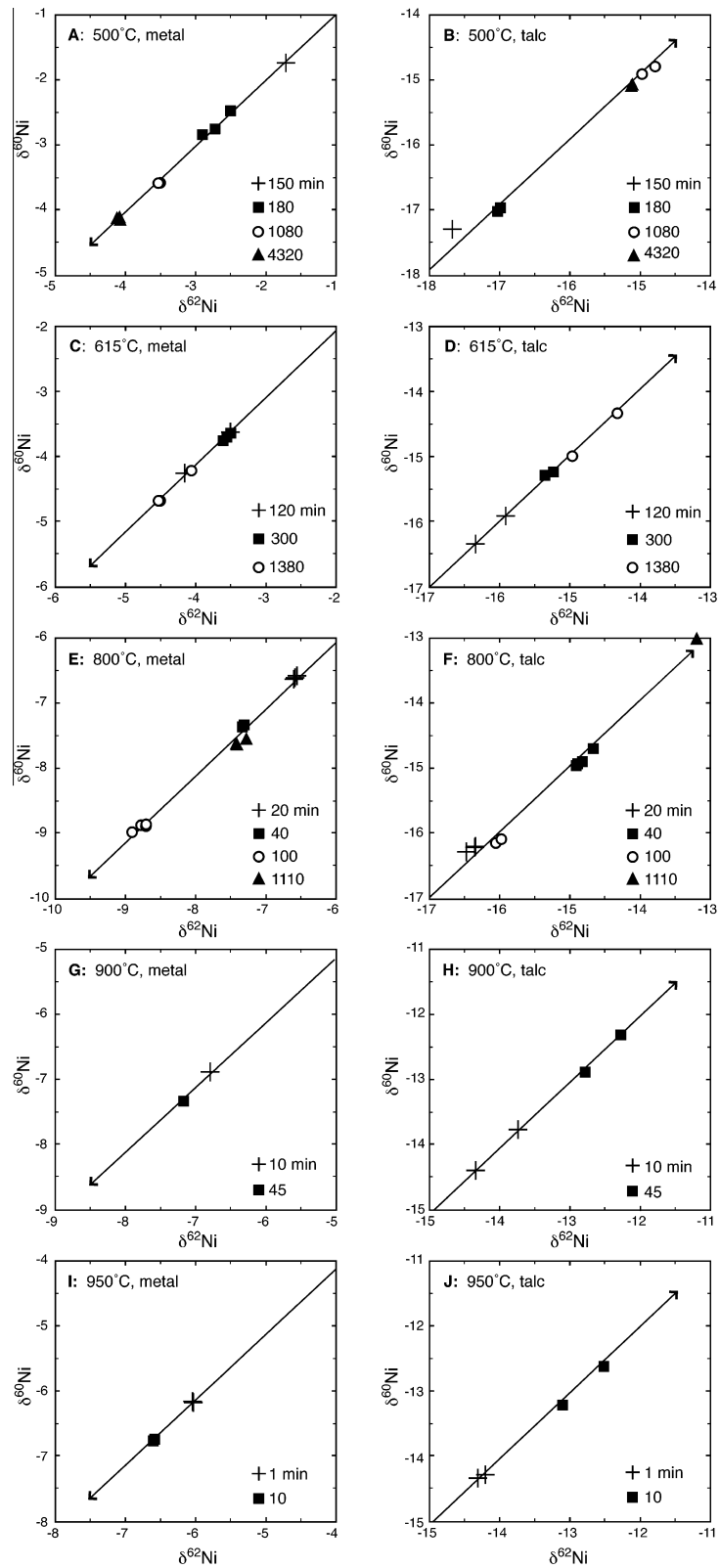
Fig. 6. Metal-talc experimental results, enlarged view. Initial compositions lay outside the field of view. Solid arrows = "new" York regressions. Arrows point toward the SFL, showing the net direction of isotopic exchange with time. Regression error envelopes are not visible at this scale. Individual error bars (±2se) are smaller than the symbols.

Table 6
Results of "new" York regression of metal-talc experimental data.

| Temperature | 500 °C | | 615 °C | | 800 °C | | 900 °C | | 950 °C | |
|---|---|---|---|---|---|---|---|---|---|---|
| Longest time (min) | 4320 | | 1080 | | 100[a] | | 45 | | 10 | |
| Phase | Metal | Talc | Metal | Talc | Metal | Talc | Metal | Talc | Metal | Talc |
| Slope | 1.010(2) | 1.000(1) | 1.008(2) | 1.006(1) | 1.008(1) | 1.002(1) | 1.009(1) | 1.001(1) | 1.008(1) | 0.998(1) |
| Y-intercept | 0.002(5) | 0.087(15) | 0.001(6) | 0.127(15) | 0.004(5) | 0.029(18) | 0.002(6) | −0.015(12) | −0.001(6) | −0.005(12) |
| Weighted mean $\delta^{60}$Ni | −2.48 | −17.20 | −2.23 | −16.57 | −5.10 | −18.28 | −2.66 | −14.86 | −2.75 | −15.12 |
| Weighted mean $\delta^{62}$Ni | −2.51 | −17.11 | −2.24 | −16.54 | −5.14 | −18.30 | −2.68 | −14.89 | −2.77 | −15.09 |
| Reduced $\chi^2$ | 28 | 691 | 6 | 34 | 20 | 76 | 58 | 42 | 2 | 138 |
| SFL intercept $\delta^{60}$Ni | −12.39(5) | −13.20(1) | −12.61(2) | −12.68(0) | −12.54(0) | −12.64(0) | −12.52(1) | −12.62(0) | −12.53(1) | −12.67(0) |
| SFL intercept $\delta^{62}$Ni | −12.15(9) | −13.72(1) | −12.57(3) | −12.71(1) | −12.44(1) | −12.64(1) | −12.41(1) | −12.59(0) | −12.43(1) | −12.69(0) |
| $\Delta^{60}$Ni$_{metal-silicate}$ | 0.23(2) | | 0.16(2) | | 0.10(2) | | 0.09(2) | | 0.13(2) | |
| $\Delta^{62}$Ni$_{metal-silicate}$ | 0.44(5) | | 0.31(5) | | 0.20(3) | | 0.18(3) | | 0.26(3) | |

[a] N20 (1110 min) was omitted (Section 4.4.1.)
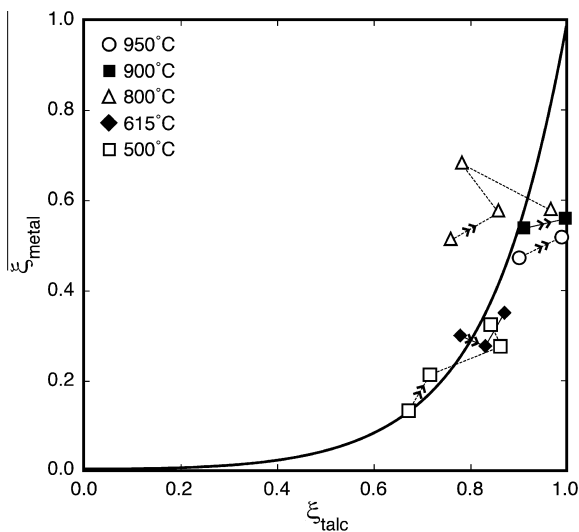


Fig. 7. Extent of exchange ($\xi$) of metal versus talc for all temperatures and times calculated using Eqs. (6) and (7) in text. Arrowheads denote increasing time. Collectively, the data were broadly consistent with an exponential function (thick solid line).



Fig. 8. Fluid-saturated phase equilibria in the system Ni—Si—O—H, 900 °C, 10 kbar. MX$^{i,f}$ = initial and final assemblages for metal-oxide experiments. MT$^i$ = initial assemblage for metal-talc experiments. MT$^f$ = final assemblage for metal-talc experiments. The x-axis is projected to $-\infty$ to approximate m(SiO$_2$) = 0. Horizontal dashed lines represent common $f$O$_2$ buffering assemblages: nickel–nickel oxide (NNO), quartz-fayalite-magnetite (QFM), and cobalt-cobalt oxide (CCO). The arrow highlights a schematic pathway to equilibrium for metal-talc experiments. Thermodynamic data references: Ni-talc (Huh et al., 2009); Ni-olivine (Hirschmann, 1991), aqueous silica (Manning 1994), all other phases (Robie et al., 1979).

isotope exchange was likely limited by self-diffusion or some other slow. In contrast, the metal-talc experiments re-equilibrated to a new phase assemblage, implying that the chemical processes attending new mineralization—e.g., precipitation, dissolution, and annealing—also facilitated Ni isotope exchange. This interpretation is consistent with a previous three-isotope study of Fe fractionation, wherein Fe isotope exchange accompanied the reaction of the unstable assemblage of hematite + fayalite + quartz + H$_2$O, to the stable assemblage of magnetite + fayalite + quartz + fluid (Shahar et al., 2008).

## 4.2. Comparison of metal-talc results to the idealized three-isotope method topology

Several key assumptions are implied by the topology of the canonical three-isotope method (Section 2.1). Below, the validity of these assumptions is discussed in the context of the present experiments. Several empirical "violations"
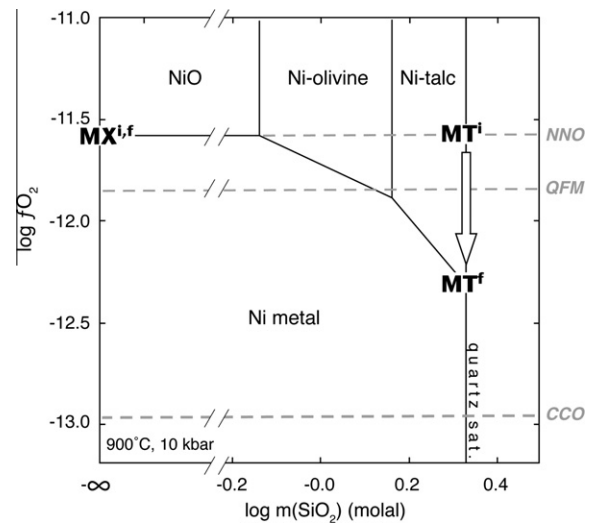
will be described; however, in most cases it will be shown that isotope equilibration can tolerate some divergence from the idealized topology (Section 4.3).

### 4.2.1. Regressions and linearity of $\delta^{60}$Ni versus $\delta^{62}$Ni data

The validity of linear extrapolation to the SFL to derive metal-talc fractionation factors was assessed by computing the deviations of the $\delta^{62}$Ni data from the values predicted from the linear regressions of $\delta^{60}$Ni versus $\delta^{62}$Ni. The deviations are defined by the expression $\delta^{62}$Ni$_{data}$ − $\delta^{62}$Ni$_{regression}$, where $\delta^{62}$Ni$_{data}$ is a measured experimental value and $\delta^{62}$Ni$_{regression}$ is a point on the regression horizontal to $\delta^{62}$Ni$_{data}$ (Fig. 9A). In the idealized case of linear behavior

of the experimental data (e.g., Fig. 1), $\delta^{62}Ni_{data}$ would equal $\delta^{62}Ni_{regression}$ for all points (zero deviation). The computed deviations were averaged for each experiment and plotted versus normalized time (time/time$_{max}$) (Fig. 9B and C). Over time, the data converge to zero (linear relationship) within uncertainties. Rather than indicating nonlinear isotopic exchange trajectories, these trends likely reflect random sampling of a population of heterogeneous grains whose compositional scatter decreases with time. Alternatively, initial scatter could be caused by minor incipient metal-talc kinetic fractionation that decays with time. In either case, convergence of the data to linearity indicates that despite initial scatter it is valid to extrapolate the exchange trajectories to the SFL in order to assess fractionation at equilibrium.

### 4.2.2. Heterogeneity in $\delta^{62}Ni$ and $\delta^{60}Ni$

The phase separates in some experiments were isotopically heterogeneous. For example, the $\delta^{62}Ni$ values for aliquots of N33 metal (615 °C) were different by almost 0.8‰, albeit along the line defining the trend towards equilibrium. Moreover, the grinding procedure used to separate metal from the silicates must have had a homogenizing effect, thus the observed variations may underestimate the true extent of isotopic heterogeneity.

However, this heterogeneity does not preclude assessing equilibrium fractionation factors in these experiments because the heterogeneity represents mixtures along equilibration trajectories in three-isotope space. Consider, for example, a characteristic diffusion length, $x$. Grain A has a radius $x$ and thus would have experienced diffusion or reaction throughout its entire volume. Grain B has a radius greater than $x$ and thus would retain a core with initial isotope ratios. The isotope ratios of B therefore represent a mixture between the initial ratios and a composition evolving towards equilibrium, and grains A and B define a mixing line between initial and final isotope ratios in three-isotope space co-linear with the starting and equilibrium compositions. Run N33 is an example of this behavior, as both N33 metal values plot on the linear regression (Fig. 6C). Similar behavior was observed at some level in every experiment.

### 4.2.3. Open system behavior

Alloying in the Au capsules indicates that the metal and talc subsystem was not closed with respect to Ni. To quantify Ni loss to the capsule, the Ni compositional profiles were fit numerically to error function expressions (Eq. EA2, electronic annex). These profiles were integrated to compute the mass of alloyed Ni and the percentage of alloyed Ni relative to the total Ni in the system (%Ni$_{alloy}$). Fig. 10A shows that %Ni$_{alloy}$ generally increased with temperature, and also increased with time at 950 °C, 800 °C and 615 °C, but not at 500 °C and 900 °C. Surface concentration of Ni ($C_s$) increased with temperature (Fig. 10B), but remained constant over time at all temperatures except 950 °C, where a significant increase occurred between 1 min and 10 min.

Diffusion coefficients ($D$) for each experiment were derived from fits to the concentration profiles in the Au cap-
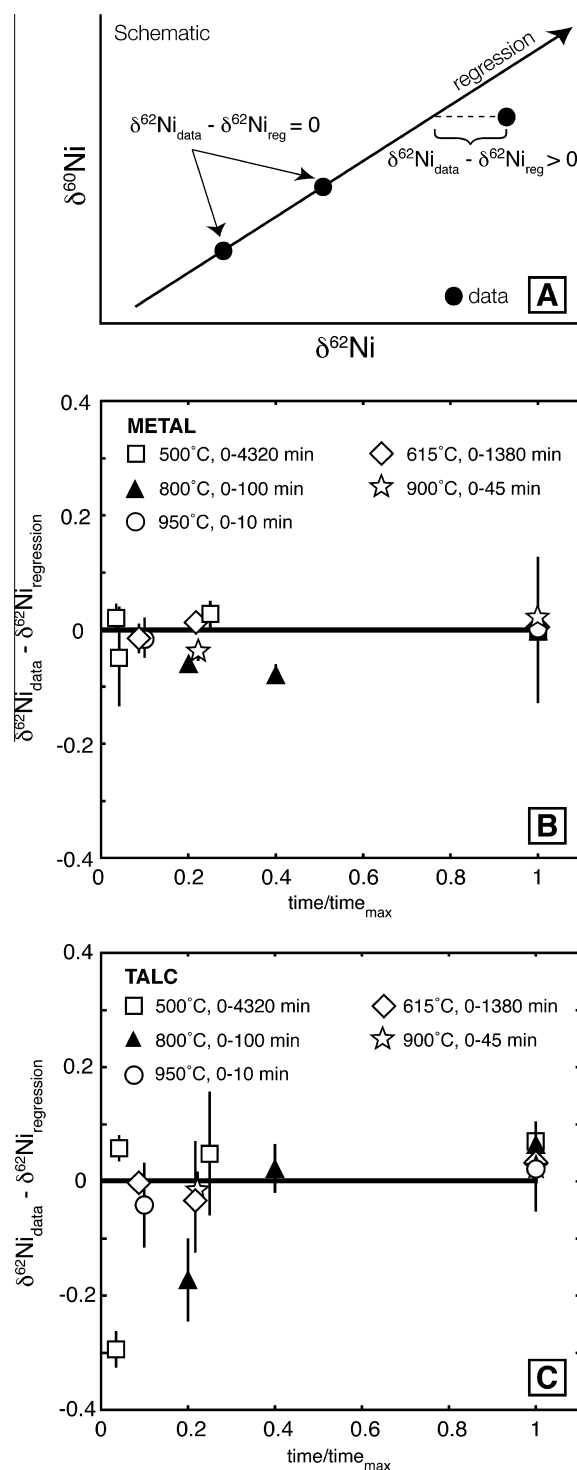


Fig. 9. Deviations of $\delta$ about the mean regression versus time. (A) Schematic illustration of the computation of the parameter, $\delta_{data} - \delta_{reg}$ (Section 4.2.1); (B) deviations versus time for metal; C) deviations versus time for talc. Experiment N20 is omitted (Section 4.4.1). For each temperature series, time was normalized to the maximum time.

sule walls (see Electronic annex). The resulting $D$ values were compared to a previously published Arrhenius relationship for lattice diffusion of Ni in Au derived from
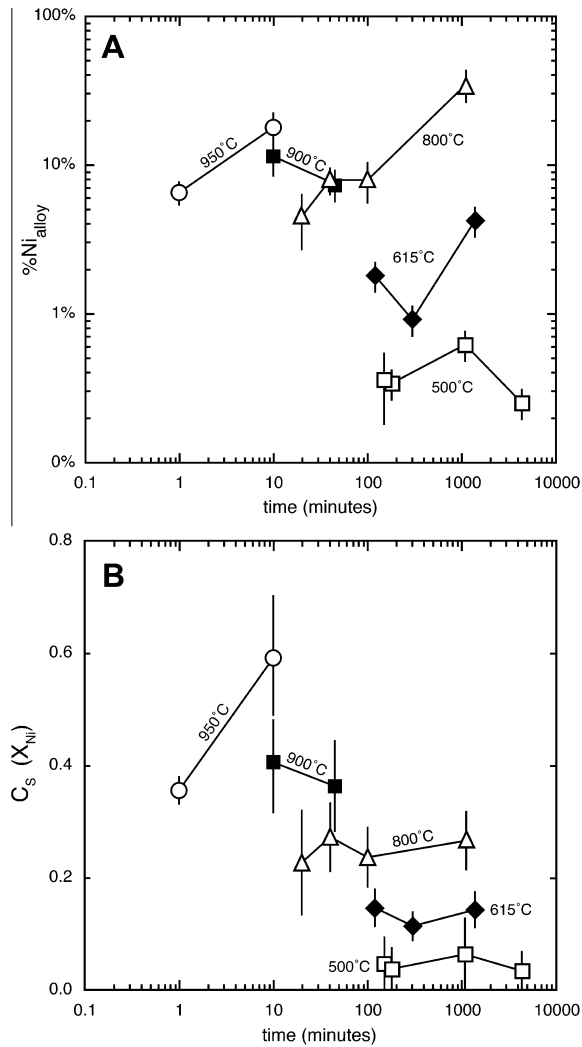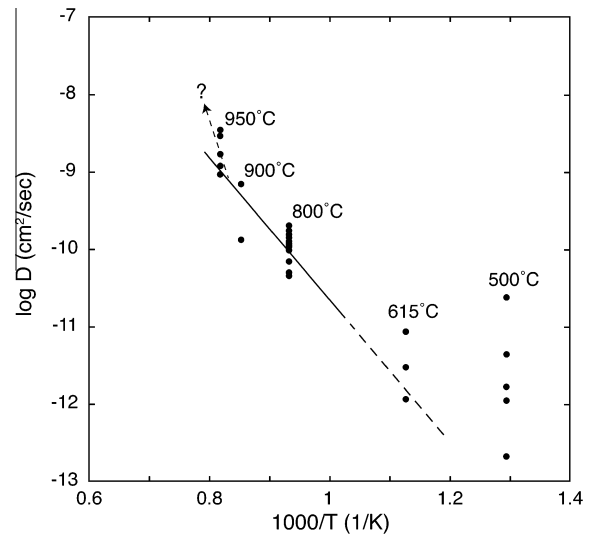
Fig. 11. Calculated diffusion coefficients (D) from metal-talc experiments versus 1000/T (from Table EA1). The solid line is a previously published Arrhenius relationship for Ni diffusion in Au from 702 °C–988 °C (solid line, Duhl et al., 1963). The dashed extension of the solid line is an extrapolation to temperatures below the Duhl et al. data. The dashed arrow reflects a possible kink in the trend above 900 °C consistent with enhanced diffusivity during premelting (Section 4.4.2).

Fig. 10. (A) Percent of total Ni alloyed with Au (%$Ni_{alloy}$) versus time and temperature for metal-talc experiments. (B) Mean concentration of Ni at inner capsule wall ($C_s$) versus time and temperature for metal-talc experiments. Error bars are ±1sd. Runs at the same temperature are connected by solid lines.

experiments at 702 °C–988 °C (Duhl et al., 1963) (Fig. 11). The D values at 800–950 °C overlap the Duhl et al. data (Fig. 11, solid line), and the D values at 615 °C overlap the extrapolated Arrhenius trend (Fig. 11, dashed line). However, the D values at 500 °C are significantly higher than the extrapolated trend and more variable than the data at the other temperatures. This suggests that extrapolating the Duhl et al. data to low temperature is invalid and/or alloying at 500 °C may occur by a process other than simple lattice diffusion alone.

### 4.2.4. Apparent shift in bulk composition

The idealized three-isotope method as depicted in Fig. 1 implies a bulk isotopic composition that does not change with time. However, loss of Ni to the Au capsule walls led to shifts in bulk compositions for the reactant phases in some cases. As an illustration, the SFL intersections used to compute the equilibrated $\Delta^{62}Ni$ values were plotted with

the initial bulk composition (Fig. 12). At 500 °C and 615 °C, the expected bulk composition is between the metal and talc compositions, consistent with the mass balance requirement that a mixture must lie on a tie line between its endmember components (Fig. 12A and B). In contrast, at 800 °C and 900 °C, the expected bulk composition does not lie between the metal and talc compositions, indicating a shift in bulk composition. Since alloying was most prevalent at these high temperatures, the shift was likely due to Ni loss to the capsule (Fig. 12C and D).

However, in all experiments, the mole fraction of Ni ($X_{Ni}$) at the outer Au capsule walls was zero, indicating that no Ni escaped from the capsule to the assembly. The bulk composition was therefore constant if the capsule walls are included, and may be defined as the weighted sum of the Ni isotope composition of the metal particles, talc, and the capsule. The topologies in Fig. 12C and D are then understood as the result of metal-talc isotopic exchange equilibrium operating as a subsystem defined by a variable apparent bulk composition that excludes the Ni lost to the capsule. Since talc was much more abundant than metal in the high temperature experiments, mass balance implies that the apparent bulk compositions in 12C and D were located very close to the talc-SFL intersections. This bulk shift to greater delta values is consistent with the diffusive loss of lighter isotopes to the capsule (Roskosz et al., 2006).

### 4.3. Extraction of metal-talc Δ values

Despite the above evidence (Section 4.2) for nonlinear exchange trajectories, isotopic heterogeneity, and open system behavior, the $\Delta^{62}Ni$ values extracted from the metal-talc experiments correlate linearly with temperature (filled
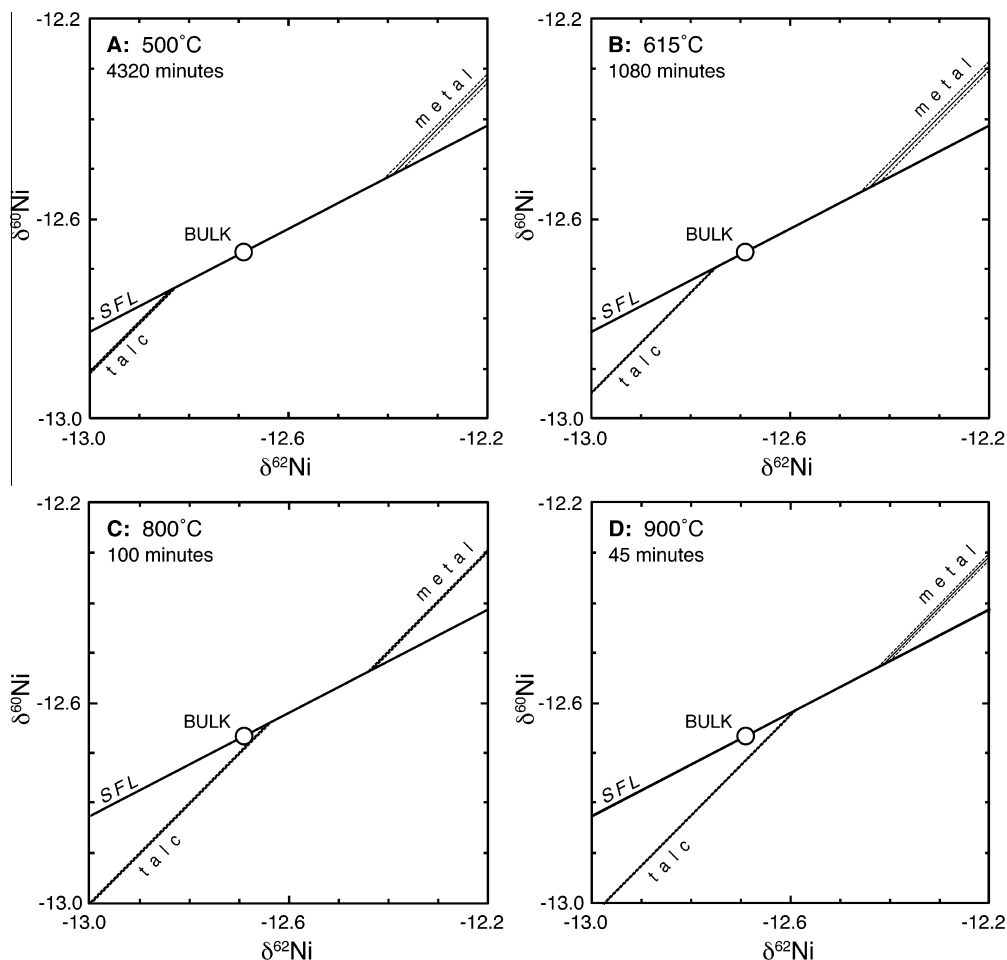
Fig. 12. Enlarged views of the intersections of the SFL with the extrapolated metal and talc regressions (light solid lines) and error envelopes (light dashed lines). Note that in some cases the error envelopes are difficult to resolve 'at this scale. Each plot shows the intersections used to compute $\Delta^{62}$Ni in the equilibrium temperature-fractionation plot (Fig. 13). Open circles = bulk composition.

symbols, Fig. 13), implying that the experimental results for the metal-talc system are consistent with Ni isotopic equilibrium between these phases. Furthermore, a free-fit New York regression of the $\Delta^{62}$Ni data versus temperature (not shown) is co-linear with the origin within the $\pm 2\sigma$ error envelope. This relationship is consistent with equilibrium temperature-fractionation because equilibrium implies zero fractionation in the limit of infinite temperature. Linear regression fixed to the origin of the $\Delta^{62}$Ni data versus temperature (filled symbols only, Fig. 13) results in the equilibrium temperature-fractionation relationship.

$$\Delta^{62}\text{Ni}_{metal-talc} = 0.26(\pm 0.02) \times 10^6 / T^2 \qquad (9)$$

where the uncertainty reflects $2\sigma$ in the slope.

There were two exceptions to the linear temperature-fractionation relationship, both denoted by open symbols in Fig. 13: the longest experiment at 800 °C (N20, 1110 min) and the experiments at 950 °C. In the following section, we argue that these experiments experienced diffusion-related kinetic fractionation that perturbed or prevented isotopic equilibrium, justifying their rejection from the temperature-fractionation regression.

### 4.4. Kinetic fractionation via diffusion at high temperature

#### 4.4.1. Rejection of experiment N20

The rejection of long-duration run N20 from the equilibrium temperature-fractionation analysis is significant because the $\Delta^{62}$Ni value derived from a regression that includes N20 (0–1110 min) is almost $3\times$ greater than the $\Delta^{62}$Ni value derived from a regression that excludes it (0–100 min) (Fig. 13). However, the $\Delta^{62}$Ni value derived from regression of the 0–100 min data at 800 °C is linearly correlative with the experiments at other temperatures, implying that the metal-talc subsystem first reached equilibrium before 100 min and then was perturbed between 100 and 1110 min.

The perturbation apparently evidenced in the long-duration run was likely caused by late-stage kinetic fractionation attending extensive diffusion of Ni° from the metal particles to the Au capsule. A recent experimental study of Fe dissolution into Pt at 1500 °C demonstrated that faster diffusion of $^{54}$Fe relative to $^{56}$Fe and $^{57}$Fe resulted in isotopically light alloy relative to a residual silicate melt (Roskosz et al., 2006). Due to the chemical and isotopic similarities between the two binary systems, the Fe-Pt
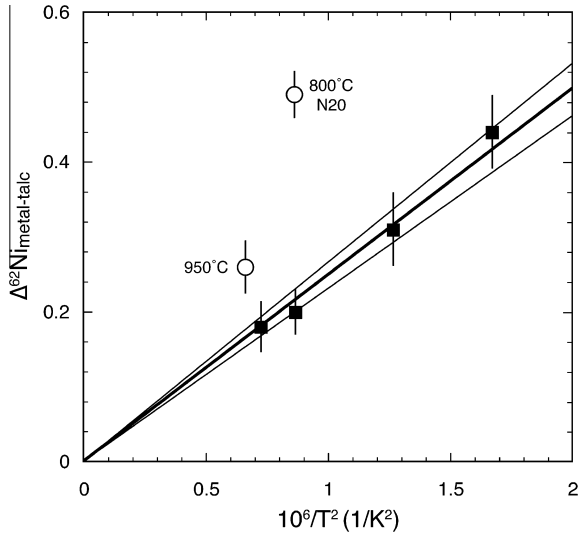
Fig. 13. Regression analyses of $\Delta^{62}Ni$ versus $10^6/T^2$. Filled squares: 500–900 °C included in regression (thick line). Open circles: experiments at 800 °C (N20) and 950 °C excluded from the regression (Section 4.4.1-2). Thin lines are $\pm 2\sigma$ confidence error envelopes of the linear regressions. Error bars on individual $\Delta^{62}Ni$ values are $\pm 2se$.
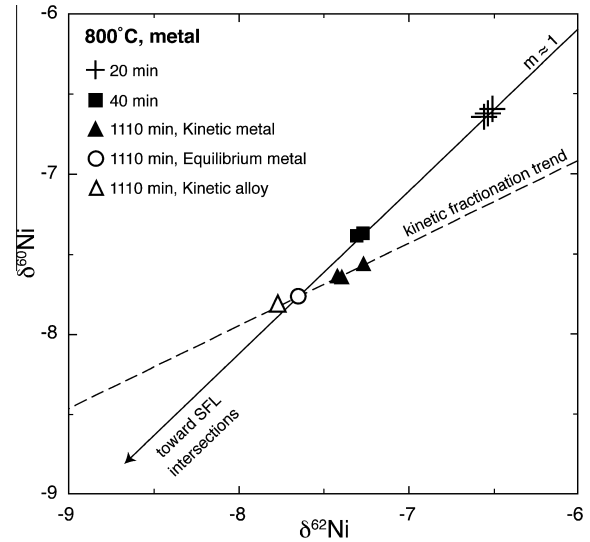


Fig. 14. 800 °C metal data from 20–1110 min showing both equilibrium trends and kinetic fractionations (Section 4.4.1). Solid arrow shows the exchange trajectory of the metal towards initial equilibrium with talc. *Kinetic Metal* (filled triangles) refers to measured metal particle compositions proposed to be controlled by kinetic fractionation during diffusive loss to Ni–Au alloy. Dashed line is the mass-dependent kinetic fractionation trend consistent with the Kinetic Metal data. *Equilibrium Metal* (open circle) is the inferred composition of metal particles equilibrated with talc obtained from the intersection of the equilibrium trajectory and the kinetic fractionation trend. *Kinetic Alloy* (open triangle) is the estimated isotopic composition of kinetically fractionated alloy computed from Eq. (10). Regression error envelopes and individual errors are not visible at this scale.

experiments are a reasonable proxy for Ni-Au, and faster $^{58}Ni$ diffusion relative to $^{60}Ni$ and $^{62}Ni$ would likely lead to an alloy relatively enriched in $^{58}Ni$ and residual metal enriched in $^{60}Ni$ and $^{62}Ni$, and erroneously high $\Delta^nNi$ values. Consistent with this hypothesis, the large percentage of total Ni (35%) transferred to the Au capsule in N20 was higher by a factor of two than in any other experiment (Fig. 10A, Table EA1).

Support for this interpretation comes from an expanded view of the 800 °C metal data showing that $\delta^nNi$ values for N20 metal were variable along a trend consistent with mass dependent fractionation (filled triangles, Fig. 14). Kinetic fractionation via diffusion would yield just such a trend. We conclude that the N20 data record diffusive loss of an isotopically lighter fraction of Ni to alloy (open triangle, Fig. 14) from an intermediate, equilibrated composition (open circle, Fig. 14). This would have biased the regression to the right, leading to an erroneously high metal-SFL intersection and $\Delta^nNi$ value.

The feasibility of kinetic fractionation was tested quantitatively using the mass balance expression

$$R^{62/58}_{\text{Equilibrium-Metal}}N_{\text{Equilibrium-Metal}}$$
$$= R^{62/58}_{\text{Equilibrium-Metal}}N_{\text{Kinetic-Metal}} + R^{62/58}_{\text{Kinetic-Alloy}}N_{\text{Kinetic-Alloy}} \quad (10)$$

where $R^{62/58}$ is the Ni isotope ratio corresponding to $\delta^{62}Ni$ and $N$ is moles of Ni. The expression describes a hypothetical distribution of Ni isotopes between three reservoirs of zerovalent Ni: *equilibrium metal* (Ni metal particles in equilibrium with talc), *kinetic metal* (Ni metal particles affected by kinetic processes), and *kinetic alloy* (Ni–Au alloy affected by kinetic processes). Implicit in Equation (10) is a two-stage isotopic exchange process: the metal first moves along the regression trajectory (slope ~1 in three-isotope space) as it equilibrates with talc, and then is pulled off

the equilibrium trajectory along a mass-dependent trend (slope = $\beta$) during later kinetic fractionation attending Ni loss to the capsule. This concept is justified empirically by noting that $\Delta^{62}Ni$ at 800 °C was consistent with equilibrium at 40 and 100 min before diverging after another factor of 10 in time in run N20, implying a metal-talc equilibration stage succeeded by a kinetic fractionation stage. Metal-talc equilibration fractionation was apparently unable to keep pace with the kinetic fractionation in the later stage, when loss of Ni to the capsule was most extensive (Section 4.5).

The $\delta^{62}Ni$ value of equilibrium metal in N20 is unknown, however its location would have lain on an exchange trajectory consistent with the equilibrated 40- and 100-min experiments. Therefore, we infer the $\delta^{62}Ni$ value of equilibrium metal was –7.78‰ (open circle, Fig. 14), estimated as the intersection of a mass dependent fractionation line fit through the N20 metal data and the linear regression of the 100-min experiment. The $\delta^{62}Ni$ value of the kinetic metal was –7.35‰, estimated as the mean $\delta^{62}Ni$ value of the 1110-min metal particles. $N$ values are from Table 3. Using Eq. (10), the value for kinetic alloy was computed to be –7.92‰ (open triangle, Fig. 14), or 0.57‰ lower than the kinetic metal particles and 0.14‰ lower than the estimated equilibrium metal. This magnitude of fractionation is reasonable in so far as it is within the range of previously observed Ni and Fe kinetic fractionation in meteorites and experiments (Roskosz et al., 2006; Cook et al., 2007;

Dauphas, 2007), and thus consistent with the interpretation that kinetic processes perturbed equilibrium in N20.

### 4.4.2. Rejection of the 950 °C experiments

In this section, we explain the reasons for rejecting the 950 °C $\Delta^{62}$Ni datum from the equilibrium temperature-fractionation regression. As in the exceptionally long run N20, kinetic fractionation during diffusion could have generated erroneously high $\Delta^{62}$Ni values in the 950 °C experiment. A key constraint is that rejection of the 950 °C runs must be reconciled with the apparent equilibration of the 900 °C experiments (Fig. 13), implying that a significant shift in chemical behavior occurred with a temperature increase of just 50 °C. The diffusion coefficient for Ni in Au at 950 °C is only twice the value at 900 °C (Duhl et al., 1963) so the temperature dependence of diffusion alone cannot account for the observed difference in the percentage of dissolved Ni: after 45 min at 900 °C, 7% of the initial total Ni was dissolved into the Au capsule. The same percentage was observed in the 950 °C experiment after just one minute, implying an unrealistic diffusion coefficient temperature dependence yielding diffusivities that are $\sim 45\times$ greater at 950 °C than at 900 °C.

Relatively rapid diffusion of Ni into Au at 950 °C relative to 900 °C may be explained by a change in the nature of the diffusion mechanism. As the temperature of a solid medium approaches its melting point, heat capacity rises rapidly, reflecting a structural change along grain boundaries to a premelted, semi-disordered state (Ubbelohde, 1957). One consequence of this subsolidus effect is an exponential increase in diffusivity along grain boundaries. All but one of the derived $D$ values at 950 °C were greater by as much as 0.5 log units than that predicted by the published Arrhenius relationship for lattice diffusion of Ni in Au, indicating a substantial increase in diffusivity between 900 °C and 950 °C (Fig. 11). This increase may be explained by a transition to faster diffusion in a region of premelting.
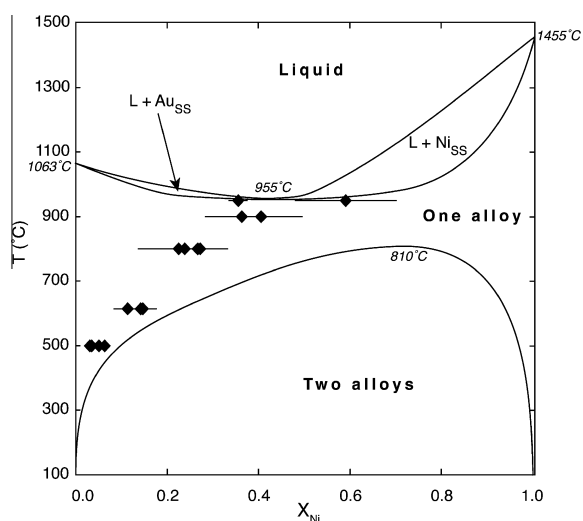
The experimental run temperature of 950 °C ± 3 °C is very close to the binary minimum melting point in the Ni–Au system at 1 bar of 955 °C (Fig. 15) (Hansen et al., 1958), lending support to the interpretation that premelting enhanced the diffusivity of Ni in Au in these runs. The 950 °C experiments were performed at 10 kbar, but $\Delta V$ and $\Delta S$ of the pure endmembers are roughly constant from 1 bar to 10 kbar, thus the temperature of the binary minimum is likely to be insensitive to pressure over this range. Therefore, the 1 bar binary solidus approximates the 10 kbar solidus, and the 950 °C experiments were likely very close to the solidus, consistent with premelting conditions.

The temperature range of the premelting region is unknown for the Ni–Au system, and poorly known for other binary metallic systems. Thermodynamic simulations in the W-Ni system suggest that the onset of grain boundary disorder may occur at temperatures as low as 60% of the eutectic temperature (Luo and Shi, 2008). A temperature of 950 °C is only $\approx 0.4\%$ below the binary minimum, indicating a reasonable overlap of the experimental conditions with an inferred premelting region.

### 4.5. An integrated schematic model for isotope redistribution

Isotopic and petrographic observations lead to a conceptual model to explain the redistribution of Ni isotopes in the experiments and provide an empirical framework for designing and interpreting future three-isotope experiments in solid–solid systems.

Important reaction pathways in the model are summarized in Fig. 16. The reaction pathways Rxn1 and Rxn2 represent nickel mass transfer between Ni metal particles and talc (e.g., Reaction (5)). To a first order, Rxn1 and Rxn2 may be viewed as an exchange couple by which metal-talc isotopic equilibrium is achieved and maintained, since both metal and talc evolved with time toward equilibrium in all experiments. Rxn3 represents dissolution of Ni° from the metal particles into the capsule wall. This pathway for Ni transfer to the Au capsule involves no change in Ni oxidation state. Rxn4 represents reduction of talc to alloy:

$$Ni_3Si_4O_{10}(OH)_2 = 3Ni^{\circ}_{alloy} + 4SiO_2 + H_2O \qquad (11)$$



Fig. 15. Binary phase diagram for Ni–Au alloy (Hansen et al., 1958) at 1 bar. Filled diamonds are Ni concentrations at the inner Au capsule walls ($C_s$) in the metal-talc experiments (Table EA1). Error bars are ±1sd.
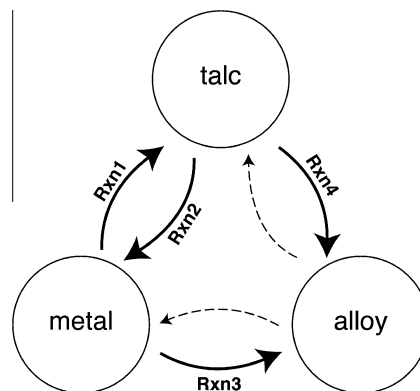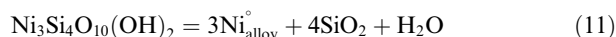


Fig. 16. Ni pathways in metal–talc experiments. Solid arrows are pathways inferred to have been active in the experiments. Dashed arrows are pathways inferred to be inactive in the experiments.

Rxn3 and Rxn4 are mechanisms by which kinetic isotope fractionation via diffusion may perturb equilibrium isotope ratios between metal and talc. No reactions depict Ni transfer from the Au capsule to metal or talc, deemed unlikely due to the uphill diffusion required against the Ni chemical potential gradients implied by the compositional profiles in the capsule walls. Note that NiO was omitted from the diagram due to the rapid and complete consumption of the oxide during early talc formation.

If we assume that the rate of Ni loss to the capsule is controlled by diffusion, then the transition from a system influenced by heterogeneous metal-talc Ni isotope equilibrium to one influenced by kinetic loss of Ni to the Au capsule is a natural consequence of the different time-dependence of the two Ni isotope exchange mechanisms. That is, the rate of heterogeneous reactions decreases with time as chemical potential gradients dissipate while the rate of diffusion of Ni is approximately constant. As illustrated schematically in Fig. 17, this implies the existence of a point, P, representing the time beyond which the rate of heterogeneous reaction falls below the rate of diffusive loss. The three distinct stages in a three-isotope exchange
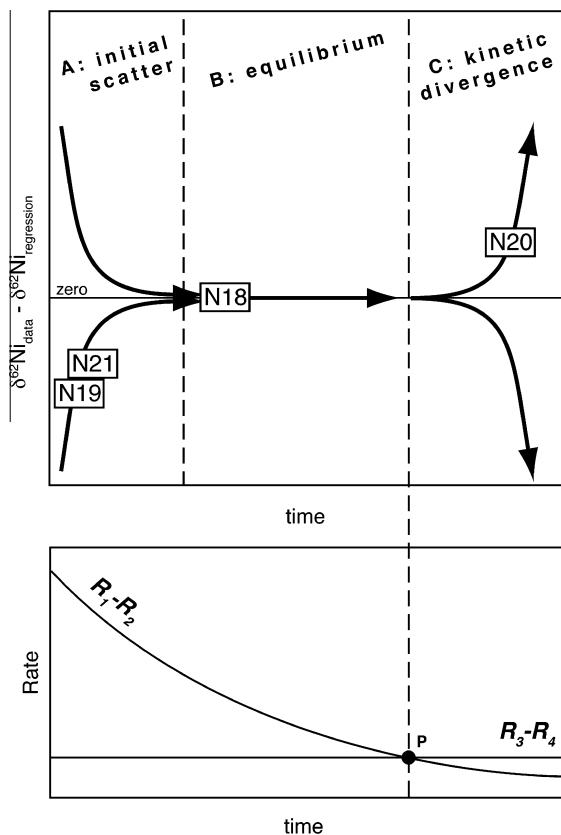


Fig. 17. Top = Schematic temporal evolution of δ variations about the mean regression in three-isotope space. Data from 800 °C metal experiments from Fig. 9B are superimposed schematically. Vertical dashed lines depict the transitions between each stage. The thin solid horizontal line is the zero-line equilibrium $\delta^{62}$Ni deviation (Section 4.2.1). Bottom = inferred schematic relative rates versus time, where $R_1$–$R_4$ are the rates of Rxn1–4 (Section 4.5). Both diagrams are isothermal.

experiment are defined in Fig. 17, where $R1$ is the rate of reaction pathway Rxn1, $R2$ is the rate of Rxn2, and so on. In the first stage (A), $R1$ and $R2$ dominate as reactants in isotopic disequilibrium undergo initial exchange toward heterogeneous equilibrium, driven by mineral dissolution and precipitation. In the second stage (B) $R1$ and $R2$ are still dominant as isotopic equilibrium is achieved and maintained between the reactant phases. Stage B is characterized by a horizontal zero-line, implying linear trends in three-isotope space towards equilibrium. In the third stage (C), beyond point P, $R1$ and $R2$ fall below $R3$ and $R4$, causing diffusive loss of Ni to the capsule to perturb the equilibrated Ni isotope ratios of the participating mineral phases. Spurious $\Delta^{62}$Ni values are therefore predicted for experiments that reach stage C.

In the context of the current study, the $\delta^{62}$Ni deviations from the regression line in three-isotope space in the 800 °C metal data (Fig. 9) are superimposed on the curves in Fig. 17 schematically for illustration. Experiments N19 and N21 occurred in stage A, but by 100 min, represented by experiment N18, the system had equilibrated isotopically. At some unknown time before 1110 min, represented by experiment N20, the system passed point P and the rate of kinetic fractionation exceeded the rate of exchange equilibration, resulting in a positive deviation in $\delta^{62}$Ni from the three-isotope linear trend and, consequently, the spurious $\Delta^{62}$Ni value seen in Fig. 13. The schematic model may also be used to explain the remaining experiments. The 500 °C, 615 °C, and 900 °C experiments converged to isotopic equilibrium in stage B, and stage C was never reached because the time required to reach point P was greater than the experimental time scales. Since the 950 °C series did not appear to equilibrate isotopically, even after just one minute, the model suggests that $R3$ and $R4$ were always greater than $R1$ and $R2$ at this temperature. Either the horizontal line depicting $R3$ and $R4$ is entirely above the curve representing $R1$ and $R2$, perhaps due to premelting, and point P does not exist at 950 °C, or point P occurred between zero and one minute.

### 4.6. Application to natural systems

Metal was enriched in the heavy Ni isotopes relative to talc in all of the experiments. This result is qualitatively consistent with reported values for the L5 Ausson meteorite (Moynier et al., 2007), wherein $\Delta^{62}$Ni$_{metal-chondrule}$ was 1.4‰. Applying the present experimental calibration (Eq. (9)), this value implies that the Ausson alloy and silicate equilibrated Ni isotopes at ∼150 °C. The present result would be consistent with a low-grade metamorphic process in this L5 meteorite if Ni isotopes were sufficiently mobile to exchange between metal and chondrules. However, olivine-spinel Fe–Mg exchange in Ausson and other L5 chondrites has been interpreted to record equilibration temperatures of 650 °C–750 °C (Kessel et al., 2007) that would lead to a much lower $\Delta^{62}$Ni$_{metal-chondrule}$ value, implying that the observed Ni isotope distribution in Ausson does not reflect an equilibrium process. Furthermore, the chondrules contained a minor amount of metal that was not separated prior to analysis (Moynier, F., personal communication), indicating that the reported $\delta^{62}$Ni

value for the chondrule may be greater than its true value. However, such an inaccuracy implies a true $\Delta^{62}Ni_{metal-chondrule}$ value that is even greater than 1.4‰, which reinforces the interpretation that Ni isotope distribution in Ausson cannot reflect equilibrium.

We are not aware of any other study reporting Ni isotope fractionation between coexisting metal and silicate. However, $Fe^{2+}$–$Ni^{2+}$ and $Fe°$–$Ni°$ are chemically similar pairs, often occurring in equivalent crystallographic sites within the common rock forming minerals. Thus, Fe isotope fractionation between metal and silicate may be a reasonable qualitative approximation to analogous Ni fractionation. With this in mind, the positive $\Delta^{62}Ni$ and $\Delta^{60}Ni$ metal–silicate fractionation values reported in the present study are qualitatively consistent with isotopically heavy Fe in metal relative to silicate in metalliferous Disko Island basalts (Sio et al., 2010), theoretical predictions using Mössbauer spectroscopy data (Polyakov and Mineev, 2000), and an equilibrium extrapolation from a Fe-Pt diffusion study (Roskosz et al., 2006).

The derived $\Delta^{62}Ni$-$1/T^2$ relationship may be used to make predictions for natural metal–silicate systems. Serpentine minerals commonly contain a few hundred ppm of $Ni^{2+}$ and often coexist with Ni–Fe alloys. At typical formation temperatures of 150 °C–300 °C, Eq. (9) implies that isotopically equilibrated alloy-serpentine fractionation could result in $\Delta^{62}Ni_{metal-silicate}$ values as large as 1.5‰.

In contrast, equilibration isotope partitioning during Earth's core formation may not generate resolvable Ni isotope variations between chondritic values and the bulk silicate Earth (BSE) unless the silicate Earth was well-mixed in Ni during separation. At 2500 K, Equation (9) implies that in $\Delta^{62}Ni_{metal-talc}$ is only 0.04‰. The resulting chondrite-BSE fractionation is calculated using simple mass balance and the assumption of a chondritic Ni isotopic composition for bulk Earth:

$$\delta^{62}Ni_{chondrite} - \delta^{62}Ni_{BSE} = \Delta^{62}Ni_{metal-silicate} f_{core} \quad (12)$$

where $f_{core}$ is the fraction of bulk terrestrial Ni in the core and in $\Delta^{62}Ni_{metal-silicate}$ is approximated by $\Delta^{62}Ni_{metal-talc}$. Using an $f_{core}$ value of 0.9 (McDonough, 2003), $\delta^{62}Ni_{BSE}$ is calculated to be <0.04‰ lower than $\Delta^{62}Ni_{chondrite}$ due to single-stage equilibration between BSE and core. This relatively small degree of fractionation relative to typical MC-ICP-MS precision suggests that resolving differences between chondrites and terrestrial mantle rocks for the purpose of searching for Ni isotope effects of core formation may be challenging. A caveat is the possibility of Rayleigh fractionation. If the process of Ni loss to metal during core formation was a Rayleigh distillation process, the depletion in heavy Ni isotopes in the residual Ni in BSE could be amplified. For a core-separation temperature of ∼2500 K, the fractionation factor from Equation (9) is 1.00004. Per mil shifts in BSE $^{62}Ni/^{58}Ni$ relative to chondrite due to Ni sequestration in the core by Rayleigh distillation is described by the equation

$$\delta^{62}Ni = 10^3((F^{\alpha-1}) - 1), \quad (13)$$

where $F$ is the fraction of total $^{58}Ni$ remaining in the silicate. Using $X_{Ni}$ as an estimate of F (i.e., $F = 0.1$), a metal–silicate equilibration temperature of 2500 K yields a measurable shift of ∼0.1 per mil for this value for F. Applicability of a Rayleigh process requires that the silicate Earth was well-mixed with respect to Ni throughout the separation process.

## 5. CONCLUSIONS

Equilibrium Ni fractionation between metal and silicate was measured using the three-isotope method, with Ni-talc and NiO as proxies for natural Ni-bearing silicates. Significant isotopic exchange was measured in the metal-talc experiments, but not in the metal-oxide experiments. This difference in behavior is interpreted a consequence of large chemical potential gradients in the metal-talc system and negligible gradients in the metal-oxide experiments. The role of heterogeneous phase equilibria implies that isotopic exchange in the experiments is the product of chemical processes such as recrystallization and dissolution.

Metal was enriched in the heavy Ni isotopes relative to talc in all experiments. Over time, scatter in the data converged to linear trends in plots of $\delta^{60}Ni$ versus $\delta^{62}Ni$, permitting extrapolation of regression analyses to the secondary fractionation line and computation of $\Delta^n Ni_{metal-silicate}$. Despite empirical evidence for nonlinear exchange trajectories, isotopic heterogeneity, Ni-Au alloying, and a variable apparent bulk composition, most $\Delta^{62}Ni$ values extracted from the metal-talc experiments correlated linearly with temperature, consistent with equilibrium. The only two exceptions to this linear correlation were high temperature experiments wherein significant diffusion of Ni metal into the Au capsule caused kinetic isotope fractionation to perturb or prevent equilibration. In both of these cases, the preferential removal of isotopically light Ni° via diffusion led to heavier residual metal particles, and $\Delta^{62}Ni_{metal-silicate}$ values greater than the equilibrium $\Delta^{62}Ni$-$1/T^2$ trend.

The experiments may place constraints on Ni isotopic variations observed in natural systems. Heavy metal relative to silicate is consistent with published Ni (and Fe) measurements. Metal–silicate fractionation in meteorites appears to be large compared with estimates for equilibration temperatures. Inter-mineral fractionation between alloy and serpentine at typical conditions of serpentinization is predicted to be as high as 1.5‰ in $\Delta^{62}Ni$. Nickel isotope fractionation attributable to core formation is not likely to result in a resolvable difference between bulk silicate Earth and chondritic $^{62}Ni/^{58}Ni$ in a single stage fractionation event, though a Rayleigh process could have resulted in a measurable difference.

## APPENDIX A. SUPPLEMENTARY DATA

Supplementary data associated with this article can be found, in the online version, at http://dx.doi.org/10.1016/j.gca.2012.02.024.

## REFERENCES

Cook D. L., Wadhwa M., Clayton R. N., Dauphas N., Janney P. E. and Davis A. M. (2007) Mass-dependent fractionation of nickel isotopes in meteoritic metal. *Meteorit. Planet. Sci.* **42**, 2067–2077.

Dauphas N. (2007) Diffusion-driven kinetic isotope effect of Fe and Ni during formation of the Widmanstatten pattern. *Meteorit. Planet. Sci.* **42**, 1597–1613.

De Laeter J. R., Bohlke J. K., De Bievre P., Hidaka H., Peiser H. S., Rosman K. J. R. and Taylor P. D. P. (2003) Atomic weights of the elements: review 2000-(IUPAC technical report). *Pure Appl. Chem.* **75**, 683–800.

Duhl D., Hirano K. I. and Cohen M. (1963) Diffusion of iron, cobalt, and nickel in gold. *Acta Metall.* **11**, 1–6.

Eugster H. P. and Wones D. R. (1962) Stability relations of the ferruginous biotite, annite. *J. Petrol.* **3**, 82–125.

Fujii T., Moynier F., Dauphas N. and Abe M. (2011) Theoretical and experimental investigation of nickel isotopic fractionation in species relevant to modern and ancient oceans. *Geochim. Cosmochim. Acta* **75**, 469–482.

Hansen M., Elliott R. P., Shunk F. A. and Research I. (1958) *Constitution of binary alloys.* McGraw-Hill, New York.

Hill P. S., Schauble E. A., Shahar A., Tonui E. and Young E. D. (2009) Experimental studies of equilibrium iron isotope fractionation in ferric aquo-chloro complexes. *Geochim. Cosmochim. Acta* **73**, 2366–2381.

Hirschmann M. (1991) Thermodynamics of multicomponent olivines and the solution properties of (Ni, Mg, Fe)$_2$SiO$_4$ and (Ca, Mg, Fe)$_2$SiO$_4$ olivines. *Am. Mineral.* **76**, 1232–1248.

Huh M. C., Lazar C., Young E. D. and Manning C. E. (2009) High-temperature equilibrium fractionation of Ni stable isotopes between metal and silicates: constraints from experimental study at 800 °C and 10 kbar. In Fall AGU conference, San Francisco.

Kessel R., Beckett J. R. and Stolper E. M. (2007) The thermal history of equilibrated ordinary chondrites and the relationship between textural maturity and temperature. *Geochim. Cosmochim. Acta* **71**, 1855–1881.

Luo J. and Shi X. M. (2008) Grain boundary disordering in binary alloys. *Appl. Phys. Lett.* **92**.

Mahon K. I. (1996) The new "York" regression: application of an improved statistical method to geochemistry. *Int. Geol. Rev.* **38**, 293–303.

Manning C. E. (1994) The solubility of quartz in H$_2$O in the lower crust and upper mantle. *Geochim. Cosmochim. Acta* **58**, 4831–4839.

Manning C. E. and Boettcher S. L. (1994) Rapid-quench hydrothermal experiments at mantle pressures and temperatures. *Am. Mineral.* **79**, 1153–1158.

Matsuhisa Y., Goldsmith J. R. and Clayton R. N. (1978) Mechanisms of hydrothermal crystallization of quartz at 250 °C and 15 kbar. *Geochim. Cosmochim. Acta* **42**, 173–182.

Matthews A., Goldsmith J. R. and Clayton R. N. (1983) Oxygen isotope fractionations involving pyroxenes – the calibration of mineral-pair geothermometers. *Geochim. Cosmochim. Acta* **47**, 631–644.

McDonough W. F. (2003) 2.15 – Compositional model for the earth's core. In *Treatise on Geochemistry* (ed. R. W. Carlson). Pergamon, Oxford, pp. 547–568.

Moynier F., Blichert-Toft J., Telouk P., Luck J.-M. and Albarède F. (2007) Comparative stable isotope geochemistry of Ni, Cu, Zn, and Fe in chondrites and iron meteorites. *Geochim. Cosmochim. Acta* **71**, 4365.

Newton R. C. and Manning C. E. (2005) Solubility of anhydrite, CaSO$_4$, in NaCl-H$_2$O solutions at high pressures and temperatures: applications to fluid-rock interaction. *J. Petrol.* **46**, 701–716.

Newton R. C. and Manning C. E. (2008) Thermodynamics of SiO$_2$–H$_2$O fluid near the upper critical end point from quartz solubility measurements at 10 kbar. *Earth Planet. Sci. Lett.* **274**, 241–249.

Polyakov V. B. and Mineev S. D. (2000) The use of Mössbauer spectroscopy in stable isotope geochemistry. *Geochim. Cosmochim. Acta* **64**, 849–865.

Robie R. A., Hemingway B. S. and Fisher J. R. (1979) Thermodynamic properties of minerals and related substances at 298.15 K and 1 bar pressure and at higher temperatures. USGS, Bulletin 1452.

Roskosz M., Luais B., Watson H. C., Toplis M. J., Alexander C. M. O. and Mysen B. O. (2006) Experimental quantification of the fractionation of Fe isotopes during metal segregation from a silicate melt. *Earth Planet. Sci. Lett.* **248**, 851–867.

Shahar A., Hillgren V. J., Young E. D., Fei Y., Macris C. A. and Deng L. (2011) High-temperature Si isotope fractionation between iron metal and silicate. *Geochim. Cosmochim. Acta* **75**, 7688–7697.

Shahar A., Young E. D. and Manning C. E. (2008) Equilibrium high-temperature Fe isotope fractionation between fayalite and magnetite: an experimental calibration. *Earth Planet. Sci. Lett.* **268**, 330.

Shahar A., Ziegler K., Young E. D., Ricolleau A., Schauble E. A. and Fei Y. W. (2009) Experimentally determined Si isotope fractionation between silicate and Fe metal and implications for Earth's core formation. *Earth Planet. Sci. Lett.* **288**, 228–234.

Sio K., Dauphas N. and Roskosz M. (2010) Can core formation in planetesimals fractionate iron isotopes? Clues from a study of metal-silicate assemblages in Disko Basalt, Greenland, 41st Lunar and Planetary Science Conference.

Steele R. C. J., Elliott T., Coath C. D. and Regelous M. (2011) Confirmation of mass-independent Ni isotopic variability in iron meteorites. *Geochim. Cosmochim. Acta* **75**, 7906–7925.

Tanimizu M. and Hirata T. (2006) Determination of natural isotopic variation in nickel using inductively coupled plasma mass spectrometry. *J. Anal. At. Spectrom.* **21**, 1423–1426.

Ubbelohde A. R. (1957) Thermal transformations in solids. *Q Rev. Chem. Soc.* **11**, 246–272.

Ulmer G. C. (1971) *Research Techniques for High Pressure and High Temperature.* Springer-Verlag.

Young E. D., Galy A. and Nagahara H. (2002) Kinetic and equilibrium mass-dependent isotope fractionation laws in nature and their geochemical and cosmochemical significance. *Geochim. Cosmochim. Acta* **66**, 1095–1104.

*Associate editor:* Mark Rehkamper